Michael Grieger

Uplink Joint Detection in a Realistic Macro Cellular Environment

Beiträge aus der Informationstechnik

Mobile Nachrichtenübertragung
Nr. 70

Michael Grieger

Uplink Joint Detection in a Realistic Macro Cellular Environment

VOGT

Dresden 2014

Bibliografische Information der Deutschen Nationalbibliothek
Die Deutsche Nationalbibliothek verzeichnet diese Publikation in der Deutschen Nationalbibliografie; detaillierte bibliografische Daten sind im Internet über http://dnb.dnb.de abrufbar.

Bibliographic Information published by the Deutsche Nationalbibliothek
The Deutsche Nationalbibliothek lists this publication in the Deutsche Nationalbibliografie; detailed bibliographic data are available on the Internet at http://dnb.dnb.de.

Zugl.: Dresden, Techn. Univ., Diss., 2014

Die vorliegende Arbeit stimmt mit dem Original der Dissertation „Uplink Joint Detection in a Realistic Macro Cellular Environment“ von Michael Grieger überein.

© Jörg Vogt Verlag 2014
Alle Rechte vorbehalten. All rights reserved.

Gesetzt vom Autor

ISBN 978-3-938860-81-6

Jörg Vogt Verlag
Niederwaldstr. 36
01277 Dresden
Germany

Phone: +49-(0)351-31403921
Telefax: +49-(0)351-31403918
e-mail: info@vogtverlag.de
Internet : www.vogtverlag.de

TECHNISCHE UNIVERSITÄT DRESDEN

Uplink Joint Detection in a Realistic Macro Cellular Environment

Michael Grieger

der Fakultät Elektrotechnik und Informationstechnik
der Technischen Universität Dresden

zur Erlangung des akademischen Grades eines

Doktoringenieurs

(Dr.-Ing.)

genehmigte Dissertation

Vorsitzender	Prof. Dr. sc. techn. habil.
	Dipl. Betriebswissenschaften Frank Ellinger
Gutachter	Prof. Dr.-Ing. Dr. h.c. Gerhard P. Fettweis
	Prof. Mikael Sternad

Tag der Einreichung:	07. Juli 2014
Tag der Verteidigung:	13. Oktober 2014

Abstract

The current annual growth rate of mobile traffic is about 70%. One important lever to cope with this demand is increasing spectral efficiency by deploying advanced network technologies. The spectral efficiency in cellular systems is limited by interference from neighboring cells. Inter-cell interference, in systems with independent base stations can only be avoided by increasing the distance at which the frequency is reused. As a result, scarce and expensive resources are wasted as frequency bands are not reused in every cell. Since inter-cell interference particularly impairs communications of users located at cell edges, it also prevents ubiquitous quality of service which to provide is another main objective of mobile operators.

It has been known for quite some time that cooperation among base stations potentially provides a means to solve the interference problem. A very powerful form of cooperation is the joint application of multi-antenna techniques at multiple base stations (in the cellular uplink referred to as joint detection). The benefit of joint detection is backed by a lot of promising theoretic results. However, the models used in this research oversimplify the complex cell coupling and other challenges in the implementation, such as hardware impairments, synchronization, and reliable control signaling. Consequently, they cannot be used for a credible assessment of communications performance in realistic cellular networks. The major testing ground during the standardization of communications methods are sophisticated system level simulations which have, in the past, however, occasionally failed to meet their purpose of accurate performance assessment. Consequently, industry players are cautious about embracing innovations that require costly upgrades of the cellular infrastructure. In order to bring innovations into the communications standards, system complexity and performance need to be assessed under real-world conditions, and simulation studies have to be accompanied by field trials that prove the maturity of a concept and provide reference data.

This thesis investigates the performance of uplink joint detection in a representative large scale testbed. To this end, a reference signal processing design for incorporating joint detection in the LTE uplink is implemented in a prototype system. Using this system, extensive multi-cell and multi-user field trials of joint detection

show that spectral efficiency is increased by 50 – 70%, on average. Especially, the performance of cell-edge users is improved (by about 300%) which increases fairness and is a significant step towards ubiquitous quality of service. A comparison of simulation and field trial measurements shows that state-of-the-art models provide accurate prediction of wireless multi-cell propagation. These results prove the accuracy of system level simulations and provide a basis for enhancements of joint detection algorithms and cellular system design in general.

Kurzfassung

Die Datenraten in Mobilfunknetzen steigen jährlich um ungefähr 70%. Ein wesentliches Mittel, um dieses Wachstum auch in Zukunft zu erhalten, ist die Steigerung der spektralen Effizienz durch den Einsatz innovativer Technologien. Die spektrale Effizienz in heutigen zellularer Netze ist grundsätzlich durch Interferenz begrenzt. In Systemen mit unabhängigen Basisstationen kann zellübergreifende Interferenz einzig verringert werden, indem der Abstand vergrößert wird, in dem Frequenzbänder wiederverwendet werden. Wird auf dieses Vorgehen und damit auf die Verschwendung begrenzter und teurer Frequenzressourcen verzichtet, dann verringert Interferenz vor allem die Übertragungsqualität von Nutzern, die sich an Zellgrenzen befinden. Eine vom Nutzerstandort unabhängige Verbindungsqualität ist allerdings ebenfalls ein wichtiges Kriterium, an Hand dessen Nutzer die Qualität eines Mobilfunknetzes bewerten.

Es ist bekannt, dass sich das Interferenzproblem potentiell durch die Kooperation von Basisstationen lösen oder zumindest abmindern lässt. Eine leistungsstarke Art der Kooperation ist die gemeinsame Anwendung von Mehrantennentechniken an mehreren Basisstationen. Diese Methode wird in der zellularen Aufwärtsstrecke als gemeinsame Detektion bezeichnet. Der prinzipielle Nutzen gemeinsamer Detektion wurde bereits in vielen theoretischen Untersuchungen gezeigt. Diese Arbeiten basieren allerdings auf stark vereinfachten Annahmen bei der Modellierung des Übertragungskanals. Darüber hinaus vernachlässigen bisherige Arbeiten wichtige Herausforderungen, die sich aus der Implementierung in einem Gesamtsystem ergeben. Zu nennen sind hier Hardwarestörungen, die benötigte Synchronisation, und die Berücksichtigung der Kontrollsignalisierung. Daher können solche Ergebnisse nicht für eine zuverlässige Bewertung der Datenkommunikation in einem realistischen zellularen System herangezogen werden. Die wichtigste Plattform für den Test und die Bewertung von Kommunikationsverfahren, die im Rahmen der Standardisierung vorgenommen wird, sind Systemlevelsimulationen. Diese haben allerdings in der Vergangenheit ebenfalls gelegentlich zu teuren Fehlbewertungen geführt. Aus diesem Grund sind die Operatoren von Mobilfunknetzen sehr vorsichtig bezüglich der Einführung innovativer Techniken, die einen teuren Umbau ihrer Infrastruktur benötigen. Um Funkstandards um innovative Techniken zu

erweitern, muss daher deren Beherrschbarkeit und Leistungsfähigkeit unter realen Bedingungen bewertet werden. Außerdem müssen Simulationsstudien von Feldversuchen begleitet werden, die den Reifegrad einer Technologie beweisen und Referenzergebnisse liefern.

Diese Arbeit untersucht die realistische Leistungsfähigkeit gemeinsamer Detektion in der zellularen Aufwärtsstrecke. Zu diesem Zweck wurden umfangreiche Feldmessungen in einem repräsentativen Testsystem durchgeführt, das sowohl mehrere Funkzellen also auch mehrere Nutzer umfasst. Die so gewonnenen Messergebnisse zeigen, dass gemeinsame Detektion die spektrale Effizienz im Mittel um ungefähr 50 – 70% erhöht. Da besonders Nutzer, die sich an Zellgrenzen befinden, von gemeinsamer Detektion profitieren (um ca. 300% erhöhte spektrale Effizienz) ergibt sich eine wesentlich gesteigerte Qualität mobiler Anwendungen. Des Weiteren wurden die Messungen mit Systemlevelsimulationen verglichen. Der Vergleich zeigt, dass heutige Simulationsmodelle eine sehr genaue Übereinstimmung mit Feldmessungen erreichen. Dieses überzeugende Ergebnis ist zugleich eine wichtige Grundlage und Referenz für zukünftige Weiterentwicklungen von CoMP Algorithmen und das Design von Mobilfunknetzen im Allgemeinen.

Acknowledgement

This thesis would not have been possible without the help and support of many others. I am very grateful to my advisor Gerhard Fettweis for his support, encouragement, and invaluable advice during the course of my thesis work. The excellent, inspiration, collaborative, and sometimes a little crazy (in a good way:) working environment at the Vodafone Chair would not exist without his guidance. Many thanks to Mikael Sternad for his support of my stay in Uppsala. To see Mikael's enthusiasm for research is a great inspiration for my work. I'm also very grateful to him for sharing and discussing his creative and innovative ideas and for being on my committee.

I'd like to thank all persons who supported setting up and operating the Dresden LTE Advanced testbed. In particular, I thank Ainoa for her skillful mastering of the SORBAS hardware and for being extremely helpful and cooperative in implementing new ideas and features; Sven-Einar for his enthusiasm in the support of field trial campaigns and skillful handling of the testbed hardware; Vincent for sharing his expertise in advanced signal processing.

Further, I like to thank Vinay Suryaprakash, Rikke Apelfröjd, Fabian Diehm, Vincent Kotzsch, Richard Fritzsche for proofreading this thesis. Their comments and advices not only helped to find errors and omissions, but also provided new perspectives and insights.

I would like to acknowledge Patrick Marsch, Eckhard Ohlmer for their supervision and advice.

Many thanks to everybody at Vodafone Group R&D in Newburry (in particular Ralf Irmer, Trevor Gil, Amy Lu) for all their insights into the real world of mobile communications.

Many thanks to Ana-Belen Martinez, Shengyan Yang, Mohammad Amro, Peter Helbig, Daniel Broß, Martin Danneberg, Stefan Boob, James Kafoe for successfully writing their thesis under my supervision.

Fabian was a great roommate and colleague, and is a great friend. Thanks for your support, teasing, ideas, and all the fun we had. Many thanks to Heike who is a

great partner for dancing Lindy Hop, but who is an even better friend.
Thanks to Chester Ditmanson for being a great friend since I came to Dresden and for guiding my "Pat-Child" Henry to become a member of the next generation of great Engineers.
Thanks to Walter for showing me how to RLRRLRLL and to Albrecht and Frank for being the party.
Parts of the research leading up to this thesis were conducted within the BMBF project EASY-C and the EU-project Artist4G. For their input and collaboration, I thank the partners of these projects, in particular Rikke Apelfröjd, Mikael Sternad from Uppsala University; Tommy Svensson and Nima Jamaly from Chalmers; and Wolfgang Zirwas from NSN.
Other parts of the research were conducted in cooperation with Huawei Shanghai. In particular I'd like to thank (Mike) Ni Ma, (Henry) Hua Huang, Yiping Wu, Lou Qunfang, and Lina Chen for great collaboration, interesting insights, and amazing visits in Shanghai.
I'm most grateful to my parents for their continuous support throughout my life which was the greatest gift anyone has ever given me.

Dresden, 1.11.2014
Michael Grieger

For my friend Fabian

Contents

Acronyms

ADC analog to digital converter . . . 39

AWGN additive white Gaussian noise . . . 37

BS base station . . . 2

CD conventional detection . . . 27

CFO carrier frequency offset . . . 39

CIR channel impulse response . . . 24

CP cyclic prefix

CoMP coordinated multi-point . . . 4

CO code orthogonal . . . 53

CRC cyclic redundancy check . . . 50

CSI channel state information . . . 37

CTF channel transfer function . . . 38

DAC digital to analog converter . . . 39

DRS demodulation reference signal . . . 52

DFT discrete Fourier transform . . . 40

eNB evolved Node B . . . 15

EVM error vector magnitude . . . 75

FDD frequency division duplex . . . 48

FEC forward error correction . . . 50

FFP Fritz-Foerster Platz (BS site) . . . 47

FT field trial (see Table A.2)

FO frequency orthogonal . . . 53

HBF Hauptbahnhof (BS site) . . . 46

Notation

General

x, X	Time / frequency domain representation of a signal
x, $\underline{x}$, $\boldsymbol{x}$	Deterministic variable - scalar, vector, matrix
$x(t)$	Time continuous signal
$x_n = x(nT_\mathrm{s})$	Time discrete signal
$x_n = \underline{x}[n]$	n-th element of a vector
$x_{n,o}$	(n,o)-th element of a matrix

Roman Letters and Arabic Numbers

$\mathbf{0}_K$	Zero matrix of size $K \times K$
a	Base station antenna index
A_g	Maximum BS antenna gain in boresight direction
$A_\Phi(\phi), A_\Theta(\theta)$	Horizontal (azimuth), vertical (elevation) antenna pattern
$\underline{b}$	Data bit stream
B	(Signal) bandwidth [Hz]
B_S, B_SC, B_c	System / subcarrier / coherence bandwidth
$\mathrm{BS}, \mathrm{BS}_{i,j}$	Base station (BS), jth BS at site i
C	Cooperation cluster size
$\underline{c}$	Coded bit stream
d	Distance
d_BP	Break point distance of LOS channels
d_CE	Distance to cell edge [m]
d_shad	Shadowing correlation distance
d_site	Inter-site distance
e	Euler's number (base of the natural logarithm)
f_c	Carrier frequency
f_SF	subframe rate
$\boldsymbol{F}_Q$	DFT matrix of size $[Q \times Q]$
$\underline{G}^\mathrm{int}$	Channel interpolation filter

$\mathbf{I}_K$	Identity matrix of size $K \times K$
$h_{\text{BS}}, h_{\text{UE}}$	BS, UE antenna height
h	Time domain CIR
$\breve{h}$	Time domain CIR after first non-zero tap
h_{s}	Height of surrounding buildings
H	Frequency domain CTF
$\breve{H}$	Frequency domain CTF associated with $\breve{h}$
HPBW_{h}, HPBW_{v}	Horizontal, vertical half power beamwidth
$\mathbf{H}$	MIMO (sub-carrier) channel matrix
$\underline{H}'$	Unfiltered estimate of the CTF
k_{B}	Boltzmann constant $k_{\text{B}} = 1.3806488 \times 10^{-}23\frac{\text{J}}{\text{K}}$
k	UE index
K, K_u	Number of UEs, number of UEs active in TTI u
l	Location index
L	Number of UE locations in a trial
LS	link separation
m	BS index
M	Number of BSs
n	Sample index
N_{ASC}	Number of active subcarriers
N_{bs}	Number of antennas per BS
$N_{\text{BS}} = CN_{\text{bs}}$	Total number BS antennas in cooperation cluster
N_{C}	Number of active data subsymbols per subframe
N_{CP}	Cyclic prefix length [samples]
N_{D}	Number of data symbols in a TTI
N_{M}	Size of discrete modulation alphabet
N_{PRB}	Number of PRB assigned to one user equipment (UE)
N_{ru}	Size of fractional frequency re-use cluster
N_{S}	Number of OFDM symbols in a subframe
N_{SC}	Number of subcarriers
NF	Noise figure [dB]
o	OFDM symbol index
P_m	Power received at BS m [dBm]
$\overline{\text{pl}}, \overline{\text{PL}}$	Average pathloss [lin, dB]
pl^{FS}	Free-space pathloss
P_{SBS}	Received power at the serving BSs [dBm]

p, P	UE transmit power [mW, dBm]
q	Subcarrier (frequency) index
Q	Number of subcarriers in an OFDM symbol
r	Achievable or achieved rate
$\bar{r}$	Ergodic rate
r_{C}	Code rate
R	Rate of an MCS
s	Snapshot index
$S = \lvert\mathcal{S}\rvert$	Number of measurements (snapshots) in one trial
SOCIR	Signal-to-outer-cluster-interference ratio
T_{s}, T_{sym}, T_{c}	Sample /(OFDM) symbol / coherence time
u	TTI index
w_{st}	Street width [m]
$x_{\mathrm{UE}}, y_{\mathrm{UE}}, z_{\mathrm{UE}}$	Coordinates of UE location
$x_{\mathrm{BS}}, y_{\mathrm{BS}}, z_{\mathrm{BS}}$	Coordinates of BS (antenna) location

Greek Letters

γ	SNR [lin]
Γ	SNR [dB]
Γ^{MI}	SINR averaged in the mutual information (MI) domain
Γ^{EVM}	SINR determined by measuring the EVM
η	Path-loss exponent
λ_{c}	Wavelength at carrier frequency f_{c}
μ	Discrete symbol timing offset
μ^{C}	Discrete CIR length
μ^{DS}	Discrete delay spread
$\mu^{\max}$	Number of discrete channel tabs
$\underline{\pi}$	Ordering (permutation) of the set $1, \ldots, K$
Φ	Azimuth angle [deg]
$\mathbf{\Phi}_V$	Noise covariance matrix
σ_V^2	Variance of complex Gaussian noise
τ	Symbol timing offset [s]
τ^{C}	CIR length [s]
τ^{DS}	Delay spread [s]
$\tau_{\max}$	Maximum channel delay [s]
Θ	Antenna downtilt (elevation) [deg]

Ψ	Shadow fading realization

Blackboard Bold Letters

$\mathbb{C}$	Set of complex numbers
$\mathbb{R}$	Set of real numbers
$\mathbb{R}^+$	Set of real, non-negative numbers

Caligraphic Letters

$\mathcal{A}$	Discrete modulation alphabet
$\mathcal{C}_k^{\mathrm{UE}}$	BS indices in UE specific cluster
$\mathcal{CN}(\mu, \sigma^2)$	Complex normal distribution with mean μ and variance σ^2
$\mathcal{D}$	Set of active data subcarriers
$\mathcal{D}'$	Set of data subsymbols in a TTI
$\mathcal{K}, \mathcal{K}_u$	Set of UEs, set of UEs active in TTI u
$\mathcal{L}$	Set of measurement locations
$\mathcal{M}$	Set of base stations
$\mathcal{N}_{\mathrm{SC}}$	Set of subcarriers
$\mathcal{P}$	Set of pilot subcarriers
$\mathcal{P}'$	Set of pilot subsymbols in a TTI
$\mathcal{P}_2$	Number of combinations of two active UEs in a snapshot
$\mathcal{P}_4$	Number of combinations of four active UEs in a snapshot
$\mathcal{R}$	Rate region
$\mathcal{S}$	Set of snapshots (measurements) in a trial
$\mathcal{S}_2$	Set of measurements with two active UEs
$\mathcal{S}_4$	Set of measurements with four active UEs
$\mathcal{Z}$	Set of sounding subcarriers
$\mathcal{Z}'$	Set of sounding subsymbols in a TTI

Operators and Functions

$*$	Convolution
$\circledast$	Circular convolution
$\hat{x}$	Estimated value
$\bar{x}$	Mean value
$(\cdot)^H$	Hermitian of a matrix (conjugate transpose)
$(\cdot)^T$	Transpose of a matrix
$(\cdot)^*$	Conjugate of a scalar, vector, matrix
$(\cdot)^\dagger$	Pseudo inverse
$\lvert\mathbf{A}\rvert$	Determinant of $\mathbf{A}$
$\lVert\mathbf{a}-\mathbf{b}\rVert$	Euclidean distance between $\mathbf{a}$ and $\mathbf{b}$
$\text{enc}(\cdot), \text{dec}(\cdot)$	Encoding, decoding function
$\text{diag}(\cdot)$	Forms a diagonal matrix from the leading diagonal of a matrix
$\mathcal{E}_{\mathsf{x}}\{\cdot\}$	Mean with respect to x
$\mathcal{E}_{\mathsf{x}}^{\text{MI}}\{\cdot\}$	Average in the mutual information domain
$\ln(\cdot)$	Natural logarithm
$\log_b(\cdot)$	Logarithm to the basis b
$\text{mod}(\cdot)$	Modulation function
$\text{Toeplitz}(\underline{a})$	Toeplitz matrix
$\text{vec}(\boldsymbol{x})$	Stacked vector of column vectors in $\boldsymbol{x}$

Remarks

One main concept used in this thesis is OFDM. To differentiate time domain and frequency domain signals, they are denoted by lower case and capital letters, respectively. Thus, e.g. x is a signal in the time domain and X in the frequency domain. Matrices are written in bold letters $\boldsymbol{x}, \boldsymbol{X}$, (column) vectors are underlined $\underline{x}, \underline{X}$, and scalars are plain letters x, X. The vector $\underline{x}_i$ refers to the ith column of the matrix $\boldsymbol{x}$, and the scalar x_i to the ith element of the vector $\underline{x}_i$. For sets, script letters $\mathcal{X}, \mathcal{Y}, \ldots$ are used. Scalar quantities in linear units are denoted by lower case letters and in logarithmic units by capital letters: e.g. p is power in mW and P in dBm.

1
Introduction

1.1. Background and Motivation

The technological innovation and improvement of cellular communications systems is linked to the constant use of popular new applications (e.g. location-based services, web browsing, social networks, gaming, and other mobile Internet applications). The relationship is bidirectional: technological innovation of cellular systems fertilizes new applications, and the great success and widespread use of applications demands an improved network performance. The current annual growth rate of mobile traffic is about 70% [CIS14]. Additionally, social networking has turned users from media consumers into content providers, which leads to a more balanced uplink / downlink traffic. To cope with the increasing demand for data traffic, advanced network technologies need to be deployed by mobile operators. Highly competitive markets, however, put a lot of pressure on costs. On the other hand, many customers are willing to pay premium prices for highly reliable and ubiquitous access to mobile services that are the pace makers of our dynamic societies. The increasing demand for data transmission should, therefore, be met with greater reliability and, yet, at minimum costs, which calls for an efficient use of the available system infrastructure and spectral resources.

A cellular system consists of two subsystems: the cellular access network and the core network. The core network — on a very abstract level — provides various communication and network management services. The access network consists of a distributed network of base stations (BSs) which provide an air interface to deliver those services to a diverse range of user equipments (UEs). This air interface is the focus of this work, in particular, the physical layer of the uplink, where UEs are transmitters and BSs are receivers. Current cellular systems like GSM, UMTS, and LTE are based on a network structure with mostly autonomous BSs, i.e., the BSs handle all tasks that are required for the communication to some assigned UEs that are, likewise, served by only one BS at a time. Often, paradigms from fixed networks have been used for communications over these links, but over time, wireless research has pioneered many novel methods for improving the link-level performance in fading channels, e.g., power control, adaptive modulation/coding, and hybrid automatic repeat request (HARQ). These methods were gradually incorporated into current standards, but interference from neighboring cells puts a strong cap on the benefits achieved. Inter-cell interference, in systems with independent BSs, can only be avoided by increasing the distance at which the frequency is reused. As a result, scarce and expensive resources are wasted as frequency bands are not reused in every cell.

It has been known for quite some time that cooperation among BSs potentially provides a means to solve the interference problem. The first technique included in a cellular communication standard, which established a simultaneous connection to more than one BS, is soft handover in UMTS. In the soft handover uplink, all BSs that actively support a connection, forward the received bit stream back to the radio network controller (RNC), along with information about the quality of the received bits. The RNC dynamically chooses the bit stream with the highest quality and, thus, benefits from diversity, which increases the likelihood of a strong signal. In an extension, which is referred to as *softer* handover, the signals at the RNC are combined constructively using maximum ratio combining (MRC).

Despite a lot of promising simulation results, such as [VVGZ94, KGPS05] being available, the application of soft handover, in the system deployed, has never shown the gains promised. Notably in the downlink, soft handover creates more interference in the system, because additional BSs transmit signals to the soft handover UEs [Lun00]. This was found out only much later, after having deployed the technology at great costs. As a consequence, soft handover was not considered in HSDPA and subsequent 3GPP standards. Interestingly, a technology which was first developed for improving the spectral efficiency of point-to-point links was later found to provide means for potentially solving the inter-cell interference problem as well: multiple input multiple output (MIMO).

1.2. From MIMO to Coordinated Multi-Point (CoMP)

MIMO techniques for wireless communication systems exploit extended degrees of freedom offered by multiple antennas on UEs and/or BSs. Among other benefits, MIMO signal processing allows decoupling of multiple data streams that are transmitted at the same time and on the same frequency resources. Ideally, capacity could be increased linearly with the number of antennas at the transmitters and the receivers [Win87, Tel99], and fading could be mitigated through diversity of uncorrelated signal paths. To bring these promises to practice, a wide range of MIMO communication schemes were developed in the last two decades [GM98]. Many of them were included in recent cellular communication standards such as LTE [Kha09] (up to 4x4 MIMO in LTE Release 8, and up to 8x8 MIMO in LTE Release 10). Today, BSs are often equipped with multiple antennas that are used for point-to-point communication with a single UE, or for point-to-multi-point communication with several UEs. The latter case is referred to as multi-user MIMO. The benefits of these schemes for cellular networks were shown in extensive measurement campaigns, e.g., [MCR10, CML+06, RMC+06]. As mentioned earlier, spectral efficiency of cellular networks is impaired by inter-cell interference. A solution to avoid inter-cell interference is the joint application of MIMO techniques at multiple BSs, as introduced in [BMWT00, SZ01, And05, KFV06, MF10]. In light of the fact that this approach requires spatially separated BSs to exchange information over a backhaul network, it is commonly referred to as network MIMO.

The general notion of network MIMO can be applied to both, the uplink and downlink. In the uplink, which is the focus of this thesis, received signals of multiple BSs (which form a cooperation cluster) are combined at a central node for joint detection (JD). Instead of simply adding the received signals constructively as in softer handover (MRC), MIMO filtering techniques separate the useful signal from interference. Thus, signal propagation across cell borders is no longer considered to cause interference, but can be used to separate UE transmissions spatially. Joint transmission (JT) applies the same notion to shape and mitigate interference in the downlink. In this case, pre-processing is used to align signals of multiple BSs at desired UE locations while suppressing signals that carry information for other UEs.

Network MIMO (in the uplink physical layer) is the main focus of this thesis, but coordination can be very useful on higher layers as well, especially for media access control. This class of coordination schemes is referred to as coordinated scheduling. It targets interference avoidance through a cooperative resource allocation within BS clusters. The umbrella term for all cooperation schemes in 3GPP is coordinated multi-point (CoMP). A comprehensive overview about recent achievements in this field is, e.g., given in [IDM+11, GHH+10]. In the following, the term JD CoMP refers to network MIMO in the uplink.

Although the behavior of conventional MIMO systems is well known, the transition of these concepts to distributed antennas is not straightforward because of two major differences, namely, hardware requirements and channel propagation characteristics. In the uplink, the concept of JD requires quantized received signals to be exchanged among BSs which causes a lot of additional traffic on the backhaul. Furthermore, the application of CoMP requires accurate frequency and timing synchronization which is not provided in today's deployments. The CoMP and the conventional MIMO channel differ mainly in the following three aspects.

- Pathloss: The links of point-to-point MIMO systems have equal average gain. While considering multiple distinct transmitters and receivers, this assumption does not hold. Distance dependent pathloss and shadowing lead to a large spread in the channel gains of the cooperation cluster.

- Fading correlation: The fading of point-to-point MIMO links is often very correlated, especially under line-of-sight (LOS) conditions. Since the correlation of fading decreases with the antenna distance, links towards distributed BSs are less likely to be correlated, which is beneficial for MIMO communication schemes that generally benefit from uncorrelated links for spatial multiplexing and diversity.

- Symbol timing: In CoMP systems, different radio propagation delays occur from one UE to multiple receiving BSs, which might impair synchronization and, thus, has the potential to degrade performance significantly.

1.3. CoMP in Practice

The costs of applying CoMP techniques are significant, and the achievable improvements of performance are difficult to assess because their study requires much more complex and comprehensive models than those typically used in the evaluation of conventional cellular systems. Prominent examples are the requirement of synchronizing all cooperating entities in time and frequency [JWS+08], multi-cell channel estimation [TSS+08, MWS02], and the consideration of backhaul delays as well as backhaul capacity constraints [MF11d]. Trading-off the benefits and costs, in terms of backhaul rate and signaling overhead for channel estimation and synchronization, requires careful joint scheduling and clustering.

In recent years, significant progress regarding these problems has been made. However, the isolated examination of individual problems is not sufficient to prove the technological maturity of ambitious CoMP concepts. One drawback in most research on CoMP is that many results are based on unrealistic assumptions, like unlimited backhaul capacity [Ven07] or overly simplified models of the cellular system [SSS07]. An interesting development is the extension of information theoretic models to more realistic network setups in [MF11d, KRF12, ZYM13]. However, a trade-off between analytical tractability and the desire to obtain realistic results is required, which usually forces one to maintain abstract, idealized assumptions in the modeling of many components while expanding some parts of the model with the goal of investigating specific issues of interest. This approach is, of course, appropriate for most communications research, but the failure of soft handover shows that a credible assessment of performance in system level simulations requires accurate and comprehensive models, which in turn need to be validated with measurements in representative scenarios.

As a result, industry players are cautious about embracing innovations that require costly upgrades of the cellular infrastructure available. In order to bring innovations into the communications standards, system complexity and performance needs to be assessed under real-world conditions, and simulation studies have to be accompanied by field trials that prove the maturity of a concept and provide reference data. These goals are driving forces behind various research projects to investigate the practicality of CoMP under more realistic system assumptions (see e.g. [IDM+11, GHH+10, DBG+10, SMG+10]).

Among such research activities, the German government funded project EASY-C and the EU project ARTIST4G stand out as the most ambitious and comprehensive. During the EASY-C project, two test beds were developed and deployed for furthering the idea of CoMP towards practical solutions which were implemented in prototype equipment, to demonstrate the practical feasibility of CoMP. Along this path, problems and challenges were identified and then solved by the collective efforts of leading mobile communication experts. One testbed was operated by Fraunhofer Heinrich-Hertz-Institut (HHI) in Berlin [JTB+09, JV11b, JFJ+10] and the other by the Vodafone Chair for Mobile Communication Systems at the Technische Universität Dresden. The latter is used in this thesis. It was designed with a focus on the investigation of a CoMP physical layer in realistic urban propagation conditions. Various BS sites were deployed to cover an area of diverse radio propagation. After being built up and running, the testbed was used in ARTIST4G as an open platform for experiment based research on various wireless innovations such as 3D beamforming, predictor antennas, and cooperative relaying.

1.4. Summary of Objectives and Thesis Overview

This thesis provides a comprehensive investigation of uplink JD-CoMP in realistic environments based on field trials in the urban LTE-Advanced testbed in Dresden. Extensive measurement campaigns were carried out and evaluated to determine the potential performance of JD in a realistic urban area. The main objectives of this work are:

1. The integration of the components required to run JD CoMP in a physical layer testbed and establishing a signal processing architecture and reference design for multi-cell channel measurements and JD CoMP reception. Achieving this goal will prove that the technical challenges of JD CoMP can be solved.

2. The investigation of multi-cell propagation in urban cellular field measurements, comparing measurement results to system level simulations for reference, and the validation of simulation parameters.

3. The evaluation of multi-cell and multi-UE field trials for comparing the performance of conventional detection (CD) algorithms and JD CoMP with respect to achievable transmission rates (on average and at the cell edge).

4. Comparing field trial results to those obtained through system and link level simulation for reference and validation of simulation results.

The remainder of this thesis is structured as follows.

Chapter 2 motivates the need for cellular field trials to demonstrate the feasibility of novel communications methods and to validate (and potentially enhance) available system simulation models. To this end, a system level simulation framework is developed for studying signal propagation and investigating the intricacies of cellular system design. The interference limitation in cellular communications is evaluated using information theoretic tools. In particular the performance of JD is compared to that of CD in several toy scenarios. Furthermore, hardware requirements and algorithms for broadband communications are discussed and major challenges in signal processing are identified.

Chapter 3 describes the testbed setup and the signal processing at UEs and BSs. The performance of the algorithms applied is investigated in link level simulations, and various CD and JD algorithms are studied in (multi-) link level models, which are more comprehensive (and realistic) than those models used the information theoretic evaluation in Chapter 2.

Chapter 4 evaluates field trial measurements regarding multi-cell propagation as well as synchronization and compares measurement results to those obtained through system level simulations. The measurements generally confirm the validity of the simulation models, but they also identify aspects that are very difficult to model accurately, especially intra-site propagation and the correlation of shadow fading.

Chapter 5 evaluates the performance of CD and JD CoMP in several extensive field trial campaigns in realistic cellular environments. The goal is to obtain a reliable measure of JD CoMP performance in comparison to communications in conventional systems. To this end, post-detection signal-to-interference-plus-noise ratio (SINR) and achieved data rates are observed. Furthermore, field trial and system level simulation results are compared for cross-validation. In addition, the field trial results help to assess the trade-off of performance gains and costs to help mobile operator to judge the benefit of the large investments required for an extensive rollout of CoMP in cellular networks. One important cost factor is the additional backhaul capacity required for using JD CoMP. Therefore, the trade-offs of available backhaul capacity and JD performance is discussed, and several methods for effective usage of the backhaul network are presented.

1.5. Notes to the Reader

This thesis covers a very wide range of topics in communications engineering. In order to keep it concise, the reader is expected to have a sound grasp of the:

- fundamentals of digital communications [Skl88];
- fundamentals of wireless and MIMO communications [Gol05],[TV05];
- fundamentals of wireless signal propagation and channel modeling [PM08];
- orthogonal frequency division multiplexing (OFDM) signal processing hardware impairments in real front-ends [HB08];
- LTE physical layer basics [DPS11].

References to the standard literature cited above will be included throughout this thesis.

CoMP is a major research topic at the Vodafone Chair. In particular, this thesis is related to two previous dissertations:

- "Coordinated Multi-Point under a Constrained Backhaul and Imperfect Channel Knowledge" by Patrick Marsch [Mar10];
- "On Multi-User Transmission in Asynchronous Cooperating Base Station Systems - Theory and Practical Verification" by Vincent Kotzsch [Kot12].

2 Fundamentals

Cellular systems are very complex due to the extensive coverage, a wide range of applications, devices, use cases (vehicular, indoor, etc.), and the complexity of the mobile wireless channel in general. Physical and media access control (MAC) layer algorithms and protocols implemented in the air interface are designed to optimize data transfer under the channel characteristics of certain environments, mobility patterns, frequency ranges etc. — of course, taking technology constraints into account. System design, development, and standardization relies on extensive simulation studies in the environments modeled. This approach is very powerful when network functions are progressed in successive incremental steps. In this case, models and their parameterization can be developed and validated in existing system implementations. The experience accumulated is a source of confidence for innovations. The approach, however, is very problematic when significant aspects of the cellular system structure are envisioned to be radically re-engineered. This is a painful lesson from the implementation of soft handover in UMTS, which performed well in simulations [VVGZ94], but failed in practice [Lun00]. Experience, thus, shows that the models available may lack important aspects of real world signal propagation and underestimate technological challenges and constraints. In order to understand the complexity of signal propagation and to understand its impact on the design of cellular systems, different simulation models are revisited in Section 2.1.

The demand for data rates provided by the air interface is constantly increasing. Since the wireless channel is a shared medium, the spectrum available is a scarce resource. In order to maximize area spectral efficiency, time and frequency resources should be reused in every cell. However, the spectral efficiency in conventional frequency reuse one networks of mostly independent BSs is limited by inter-cell interference. Section 2.2 motivates CoMP as a groundbreaking technique with the potential to resolve the problem of inter-cell interference and, thereby, increase spectral efficiency significantly. To this end, CoMP completely changes the fundamental notion that each UE communicates only with a single serving BS. Instead, multiple clustered BSs cooperate to jointly serve UEs that would otherwise, in a conventional system, cause substantial mutual interference. The benefits of this approach are shown for the uplink where the received signals of distributed BSs are combined for JD. The investigations in this chapter are based on the information theoretic models.

Section 2.2 also provides simulation results that investigate the performance of conventional and JD CoMP communication schemes with regard to different system and channel parameters for narrowband channels. Cellular systems for data communication, however, are broadband systems. A modulation scheme used in many modern broadband systems is OFDM. OFDM transforms a channel into multiple orthogonal subcarriers which can be used to simplify physical layer algorithms, especially for MIMO systems. However, the notion of orthogonal subcarriers relies on stringent assumptions related to synchronization and fading, which do not necessarily hold in CoMP systems. These aspects are discussed in Section 2.3 which also shows the assumptions, limitations, and constraints of the results presented in this thesis.

2.1. Signal Propagation Models and their Limitations

In a macro-cell system, BSs are deployed at sites which are placed with rather regular spacing. The inter-site distance is influenced by traffic demand (user population) and availability of suitable site locations. Typical values are between a few hundreds of meters in urban areas with high population and thousands of meters in remote rural areas. A commonly used model for a cellular network is a regular grid of hexagonal cells — so called honeycomb patterns — as shown in Figure 2.1. Signal propagation in this model is considered in this section. While Section 2.1.1 describes modeling of average pathloss for LOS and non-line-of-sight (NLOS) scenarios in a honeycomb model with omni-directional antennas (Figure 2.1a), the impact of BS antenna design and sectorization (Figure 2.1b) is discussed in Section 2.1.2.

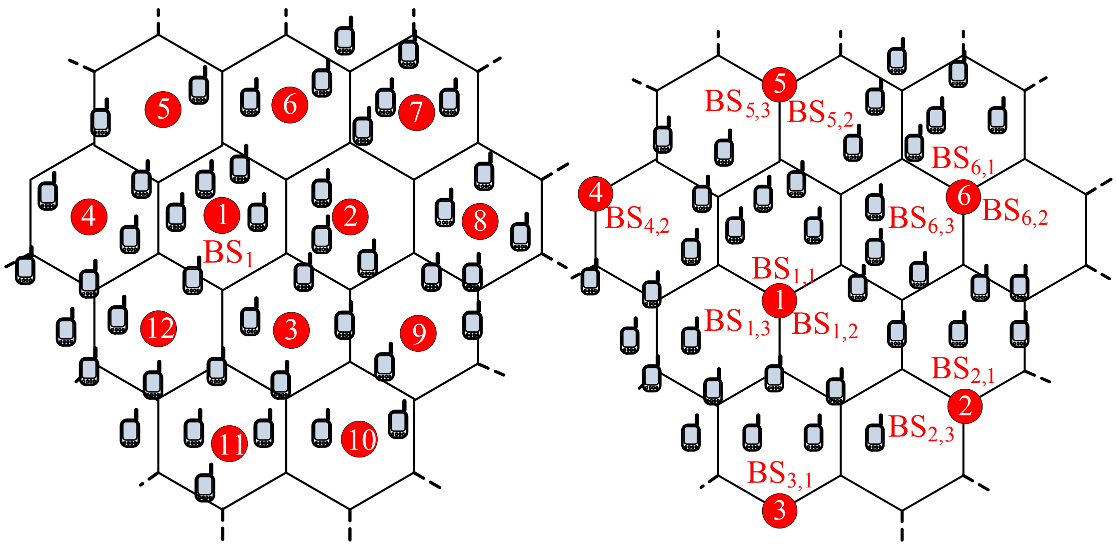

(a) Omni honeycomb model. **(b)** Sectorized honeycomb model.

Figure 2.1.: Hexagonal models of cellular systems. The numbered dots indicate BS sites.

For theoretical analysis and simplified simulations, often, subsystems with few UEs and BSs are considered, as shown in Figure 2.2. As long as sufficiently accurate time and frequency synchronization of all UEs in a cell can be achieved, orthogonal channels are established on different time and frequency resources. This reduces the complexity of a cellular system as shown in Figure 2.2a, where only those UEs that transmit simultaneously in the same part of the spectrum are considered (one UE per BS in this example). A further simplification is the consideration of networks with few BSs which are strongly coupled by inter-cell interference, as shown in Figure 2.2b for a two-BS-setup. Such toy scenarios are convenient for studying the impact of specific parameters and effects in a well controlled environment.

2.1.1. Average Pathloss for LOS and NLOS Channels

In wireless communications, the transmitted signal is broadcasted, and only a small portion of the transmitted energy is also captured at the receiver due to pathloss. This section explains pathloss models for different topologies. In a first step, propagation in free-space is explained where pathloss is a deterministic distance depending quantity. Afterwards models for average pathloss in terrestrial topologies is discussed where propagation is impacted by the complicated interplay of reflection, diffraction, and propagation in the environment around the

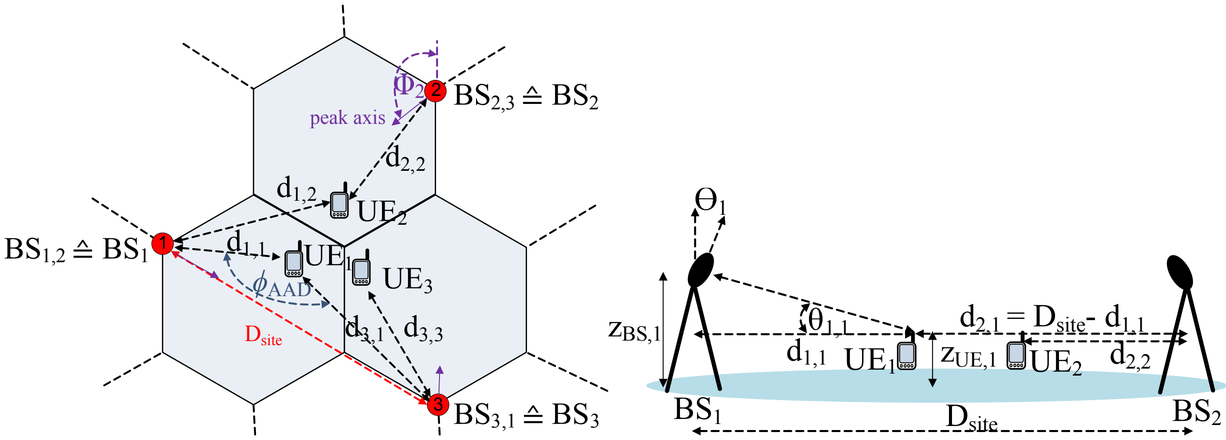

(a) Subsystem with few BSs and UEs that transmit on the same resources.

(b) Toy scenario with two BSs.

Figure 2.2.: Simplified cellular models of two or three cells established at different sites. Only those UEs that transmit on the same spectral resources are shown. Outer cluster interference can be modeled by an additional noise term. The reader is referred to the table inserted before Chapter 1 for details on the notation used throughout this thesis.

transmitter and the receiver.

2.1.1.1. Free-Space Propagation

Figure 2.1a shows a honeycomb model of a cellular system where the BSs are assumed to be equipped with omni-directional antennas. Each cell is controlled by one BS that commands the allocation of spectral resources in the corresponding cell area. It is, therefore, referred to as serving BS of all UEs in the cell.

The formation of a regular cell pattern is based on the assumption that the distance dependent pathloss is independent of the surrounding topology. In free-space, the received power of UE_k at BS_m is given by

$$p_{m,k} = \frac{p_k}{\mathrm{pl}^{\mathrm{FS}}_{m,k}}, \tag{2.1}$$

where p_k is the transmit power of UE_k. Therein, the free-space pathloss

$$\mathrm{pl}^{\mathrm{FS}}_{m,k} = \left(\frac{4\pi d_{m,k}}{\lambda_{\mathrm{c}}}\right)^2 \tag{2.2}$$

depends on the carrier wavelength λ_{c} and the distance between BS m (located at the coordinates $(x_{\text{BS},m}, y_{\text{BS},m}, z_{\text{BS},m})$) and UE k (located at $(x_{\text{UE},k}, y_{\text{UE},k}, z_{\text{UE},k})$):

$$d_{m,k} = \sqrt{\left(x_{\text{BS},m} - x_{\text{UE},k}\right)^2 + \left(y_{\text{BS},m} - y_{\text{UE},k}\right)^2 + \left(z_{\text{BS},m} - z_{\text{UE},k}\right)^2}. \tag{2.3}$$

Figure 2.3a shows the free-space pathloss simulated at the serving BS in an omni-honeycomb system where the BSs are equipped with omni-directional antennas. The simulation parameters are listed in Table A.1. They are in line with the environment of the field trial setup, which is the subject of the following chapters. The inter-site distance $d_{\text{site}} = 750$ m which is the case in all simulations that will follow.

While free-space propagation is a justified model for stationary point-to-point links that operate under clear LOS (full opening of the first Fresnel zone [Has08, p. 79ff.]), it is not valid in cellular mobile communications for the following reasons:

1. Obstructions of the LOS (shadowing) lead to an increase in the average pathloss as discussed in (the upcoming) Section 2.1.1.2.

2. BSs are equipped with directional antennas in order to establish multiple cells per site, re-use spectrum, and increase area capacity, as discussed in Section 2.1.2. Since the orientation of these BS antennas is fixed, and the same orientation is used to communicate with all UEs in the cell area, a location dependent antenna radiation intensity has to be considered.

3. Shadowing leads to large-scale fading of the pathloss which is correlated over distances on the order of the size of major objects in the propagation environment as discussed later in Section 2.1.3.

4. Multi-path propagation leads to small-scale fading as discussed subsequently in Section 2.1.4.

2.1.1.2. Empirical Pathloss Models

In real environments, signal blocking due to surrounding buildings and geographical structures in the transmission path results in less predictable signal propagation and a reduction in the average received power. Empirical models of the average pathloss for particular landscapes and transmission parameters were designed based on extensive measurement campaigns, such as COST-231 Hata [Hat80] and Walfish-Ikegami [WB88, IYTU84, CA99]. A very good overview is given in [Mol10,

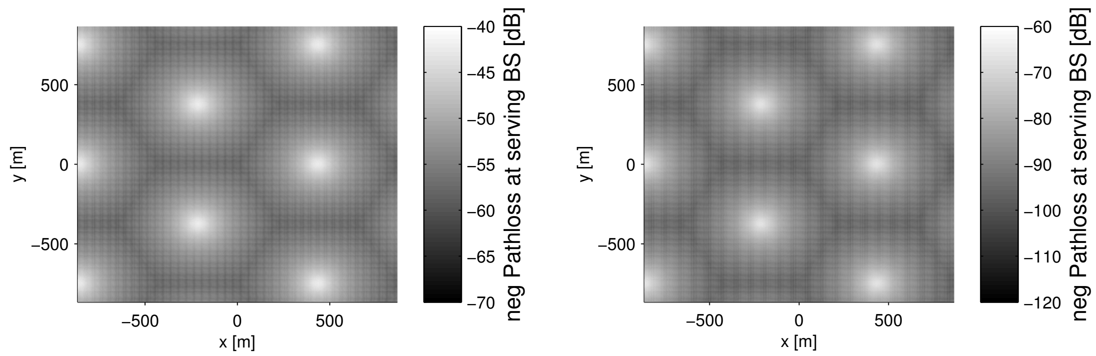

(a) Free-space pathloss (SL 1 in Table A.1)

(b) 3GPP ITU NLOS pathloss (SL 2 in Table A.1)

Figure 2.3.: Pathloss in omni honeycomb model. Note the different scales which reflect the increased NLOS pathloss.

Appendix 7.6.1]. In logarithmic units, these models of the average pathloss $\overline{\mathrm{PL}}_{m,k}$ are typically of the form

$$\overline{\mathrm{PL}}_{m,k} = A + 10\eta \log_{10} d_{m,k} \text{ [dB]}, \tag{2.4}$$

where A and η depend on characteristic parameters of the propagation environments, such as BS antenna height $z_{\mathrm{BS},m}$, UE antenna height z_{UE}, street width w_{st}, height of surrounding buildings h_{s}, and carrier frequency f_{c}. The parameter η is referred to as the pathloss exponent. In this work, the macro cell ITU-Advanced pathloss model is used [3GP10, Section B.1.2.1], which is valid in the frequency range between 2 – 6 GHz. For a NLOS channel is given by

$$\begin{aligned}
\frac{\overline{\mathrm{PL}}_{m,k}^{\mathrm{NLOS}}}{[\mathrm{dB}]} &= 161.04 - 7.1 \log_{10}\left(\frac{w_{\mathrm{st}}}{[\mathrm{m}]}\right) + 7.5 \log_{10}\left(\frac{h_{\mathrm{s}}}{[\mathrm{m}]}\right) \\
&- \left(24.37 - 3.7\left(\frac{h_{\mathrm{s}}}{z_{\mathrm{BS},m}}\right)^2\right) \log_{10}\left(\frac{z_{\mathrm{BS},m}}{[\mathrm{m}]}\right) \\
&+ \underbrace{\left(43.42 - 3.1 \log_{10}\left(\frac{z_{\mathrm{BS},m}}{[\mathrm{m}]}\right)\right)}_{B_{\mathrm{NLOS}}=10\eta_{\mathrm{NLOS}}} \left(\log_{10}\left(\frac{d_{m,k}}{[\mathrm{m}]}\right) - 3\right) \\
&+ 20 \log_{10}\left(\frac{f_{\mathrm{c}}}{[\mathrm{GHz}]}\right) - \left(3.2\left(\log_{10}\left(11.75 \frac{z_{\mathrm{UE}}}{[\mathrm{m}]}\right)\right)^2 - 4.97\right).
\end{aligned} \tag{2.5}$$

The equation shows a higher pathloss exponent compared to free-space propagation, e.g., $\eta_{\mathrm{NLOS}} = 3.82$ at $z_{\mathrm{BS},m} = 50$ m. The difference between NLOS and

LOS propagation can be seen when comparing Figure 2.3a and Figure 2.3b, which show LOS and NLOS pathloss in a honeycomb model, respectively. For example, at the cell edge at a distance of 350 m from the BSs, NLOS pathloss is about 40 dB higher than LOS pathloss.

Measurement campaigns in real environments also show that LOS pathloss cannot be accurately modeled using (2.2). One reason is because there is no clear separation between LOS and NLOS due to the fact that objects in the Fresnel zone might not block the LOS while still having a strong impact on the propagation conditions [Par00]. Even LOS signal propagation in a completely flat terrestrial scenario is potentially impaired by an additional ray reflected from the ground. The two rays in this channel model mutually cancel each other out, if $d_{m,k}$ is greater than a break point distance $d_{\mathrm{BP},m} = 2\pi z_{\mathrm{BS},m} z_{\mathrm{UE}} f_{\mathrm{c}}/c$, resulting in a greater pathloss exponent $\eta = 4$ [Gol05, Section 2.4.1]. The ITU-Advanced channel model for LOS propagation in urban macro cells is given in Equation (A.1) of the appendix. In this model, a pathloss exponent of $\eta_{\mathrm{LOS},1} = 2.48$ is applied below d_{BP}, and another $\eta_{\mathrm{LOS},2} \geq 4$ beyond this distance. This is actually a very simple model of ground wave propagation. The reader is referred to [Wai98] for a detailed overview of additional effects such as so called Norton surface waves [Nor41].

2.1.2. Sectorization and Antenna Patterns

The cellular setup of Figure 2.1a, where a single cell is established per site, assumes the use of omni-directional (isometric) antennas. A more common setup is shown in Figure 2.1b. Here, multiple cells — in this context also referred to as sectors — are hosted at one site. Each cell is controlled by a single BS[1]. Sectorization is employed in order to reduce the total number of site locations for economic reasons. It relies on directional antennas which are designed such that the spatial dissipation of power is constrained to a certain angular range.

2.1.2.1. Antenna Specification

An overview of current BS antenna technology is given in [Sch] and [3G 10]. A complete picture of the antenna's directivity is given by the radiation pattern. Separate patterns of the horizontal (azimuth) $A_\Phi(\phi)$ and the vertical (elevation) $A_\Theta(\theta)$ are typically measured in an anechoic chamber and displayed in an antenna data sheet. As an example, Figure 2.4 shows these radiation pattern of the Kathrein 80010541 antenna [KG].

[1]In 3GPP terminology, one evolved Node B (eNB) may control several cells at one site.

Due to the intricacy of these patterns, several parameters are defined for their characterization. The main lobe is in the direction of strongest radiation; all other lobes are side lobes. The (main beam) peak axis is the direction of maximum radiation intensity. It is specified by the angle Φ in the azimuth, and the angle Θ in the elevation plane, where Θ is also referred to as downtilt (see Figure 2.2). Along the peak axis, signal radiation/reception intensity is increased by a gain of A_g [dBi] compared to an isometric antenna. The main lobe is further characterized by the angles relative to the peak axis, where the radiation intensity drops by 3 dB. The difference between these angles is called half power beam width (HPBW).

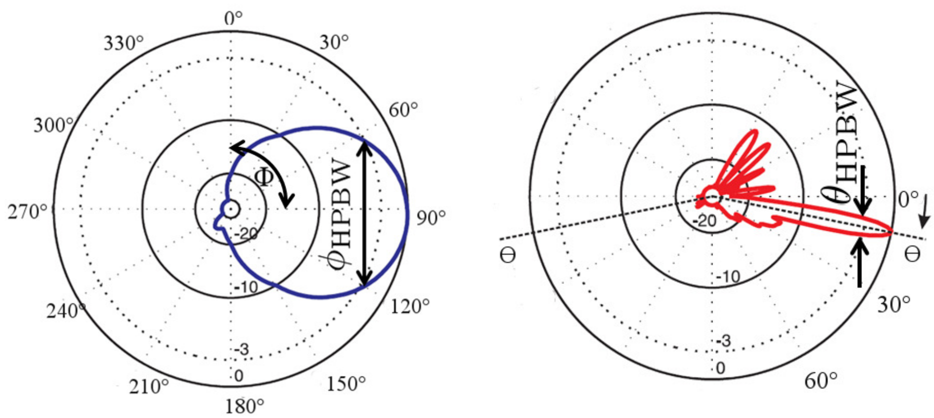

(a) Azimuth $A_\Phi(\phi)$ **(b)** Elevation $A_\Phi(\theta)$

Figure 2.4.: Azimuth and elevation patterns of KATHREIN 80010541 base station antenna at 2.6 GHz carrier frequency [KG].

In order to maximize area spectral efficiency, time and frequency resources should be reused in every sector. Therefore, antenna patterns in conventional networks are chosen to be non-overlapping (within the limits of practical feasibility) to avoid inter-sector interference. The azimuth HPBW of a typical BS sector antenna is about $60°$ for a sectors opening of $120°$ and three non-overlapping sectors per site, i.e., the so called three fold sectorization.

At the UE, low gain (or isometrical) antennas are used because the device is typically pointed in random directions. The antenna radiation intensity is typically modeled to be a constant value (isometric antenna). While, e.g., $A_g = -1$ dBi is used in 3GPP [3GP10], no gain ($A_g = 0$ dBi) is assumed here and, thus, this factor can be neglected.

2.1.2.2. Impact of Antenna Patterns

In the following, the UEs transmit with a fixed power $P = 10\log_{10}(p/1\text{ mW})$ dBm. Taking the antenna pattern into account, the general relationship between P and the power received at BS$_m$ is

$$P_{m,k} = P + A_m(\phi_{m,k}, \theta_{m,k}) - \overline{\text{PL}}_{m,k}\ [\text{dBm}], \tag{2.6}$$

where $A_m(\phi, \theta)$ is the antenna gain at a certain orientation between the particular UE and the m^{th} BS. The angle ϕ describes the horizontal while θ expresses the vertical deviation from the antenna peak axis. Depending on the UE and BS location, these angles are determined by

$$\theta_{m,k} = \tan\left\{\frac{\sqrt{\left(x_{\text{BS},m} - x_{\text{UE},k}\right)^2 + \left(y_{\text{BS},m} - y_{\text{UE},k}\right)^2}}{z_{\text{BS},m} - z_{\text{UE},k}}\right\} - \Theta_m, \tag{2.7}$$

$$\phi_{m,k} = \tan\left\{\frac{x_{\text{BS},m} - x_{\text{UE},k}}{y_{\text{BS},m} - y_{\text{UE},k}}\right\} - \Phi_m, \tag{2.8}$$

where Φ_m determines the orientation of the antenna main beam in the azimuth. Different ways to create 3D antenna patterns $A_m(\phi, \theta)$ are described in [AGdA02, GCF$^+$01]. A conventional one, also used herein, is adding the gains of the horizontal and the vertical pattern with equal weights as described in [TWS$^+$09, II. A]:

$$A_m(\phi, \theta) = A_{\Phi,m}(\phi) + A_{\Theta,m}(\theta). \tag{2.9}$$

The geometric derivation of the radiation intensity at a particular location (defined in Equation (2.6)) is accurate only for LOS locations. A more involved propagation over clutter model for NLOS scenarios is discussed in [CL08]. The accuracy of the two models was compared in outdoor field measurements in the Dresden testbed [1]. For the test locations, which are characterized by surrounding buildings of relatively low height (compared to the BS antenna locations) placed in rather large distance, Equation (2.6) was found to be a good model while [CL08] predicted the antenna pattern to be impacted too much by surrounding buildings. However, for other application scenarios which are characterized by a BS height similar to that of surrounding rooftops, the propagation over clutter model is expected to provide the more realistic results because it takes street canyon effects (described in [PM08, Chap. 8]) into account. The drawback of models, such as [CL08], is, therefore, that they need to be parameterized very carefully with respect to the actual propagation scenario. This is the reason why they are not used in standard models as, e.g., used by 3GPP. Therein, the impact of NLOS on antenna patterns is considered to be accounted for by the shadowing model presented in Section 2.1.3. Other site specific factors, which might affect the antenna pattern significantly, are objects in close proximity to the antenna, such as the mounting pole or the roof edge. The resulting near field propagation differs substantially from that observed in an anechoic chamber.

2.1.2.3. Antenna Downtilt

The coverage of individual BSs is intentionally reduced in urban areas for shorter distances of frequency reuse. One potential means for reducing coverage is lowering transmit power, but this approach causes poor service inside buildings and in shadowed areas. For these reasons, the preferred solution is to exploit degrees of freedom in antenna design for the purpose of coverage reduction. A typical BS antenna consists of multiple dipoles that are placed in a single or multi-column planar array structure with mutual spacing of about $\lambda_\mathrm{c}/2$, where $\lambda_\mathrm{c} = \frac{c_\mathrm{light}}{f_\mathrm{c}}$ is the wavelength at the carrier frequency f_c, and c_light the speed of light. In theory, amplitudes and phases of the feeding signals can be adjusted to produce flexible radiation patterns [Col02, GUY88]. Today's state of the art electrical tilting technology does not achieve this flexibility, but allows controlling the antenna downtilt Θ by an appropriate adjustment of the feeder cable length of all internal dipoles through a mechanical phase shift network which is steered by an electric motor.

2.1.2.4. Simulation Results

This section presents simulation results on the impact of BS antenna patterns in cellular systems. An appropriate metric for signal quality at the receiver is the signal-to-noise ratio (SNR). Neglecting interference, thermal noise is the major source of distortion at the antenna. Across the signal bandwidth B, it has a power of

$$P_\mathrm{n} = 10\log_{10}\left(\frac{k_\mathrm{B}TB}{1\ \mathrm{mW}}\right)\ [\mathrm{dBm}] \tag{2.10}$$

at temperature T, where k_B is the Boltzmann constant. The SNR of UE_k at the antenna of BS_m is given by $\Gamma^\mathrm{in}_{m,k} = P_{m,k} - P_\mathrm{n}$ [dB]. However, active components in the analog receiver chain cause additional random distortions. These reduce the

SNR by some noise figure NF which in dB is given by

$$\Gamma_{m,k} = \Gamma^{\text{in}}_{m,k} - \text{NF}. \tag{2.11}$$

The noise figure combines the effects of all active components as well as filtering and cable losses before the low noise amplifier (LNA) [AEH+63]. In the following, a noise figure of $\text{NF} = 5$ dB is assumed in compliance with [3GP10, Table A.2.1.1.4-3.]. The SNR at NLOS locations in a sectorized honeycomb model is shown in Figure 2.5. A generic macro cell antenna pattern, as defined in [3GP10, Table A.2.1.1-2], is used in Figure 2.5a, and the Kathrein 80010541 antenna pattern is used in Figure 2.5b. The plots show that the impact of different antenna patterns are most noticeable at a distance close to the BS.

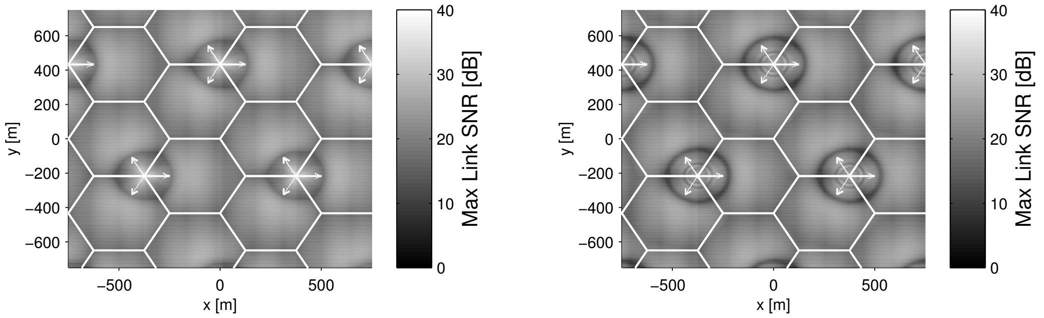

(a) Generic 3GPP antenna pattern [3GP10] (SL 3 in Table A.1)

(b) Kathrein 80010541 antenna pattern (SL 4 in Table A.1)

Figure 2.5.: Sectorized honeycomb model with different antenna patterns. In the following, the Kathrein 80010541 is used.

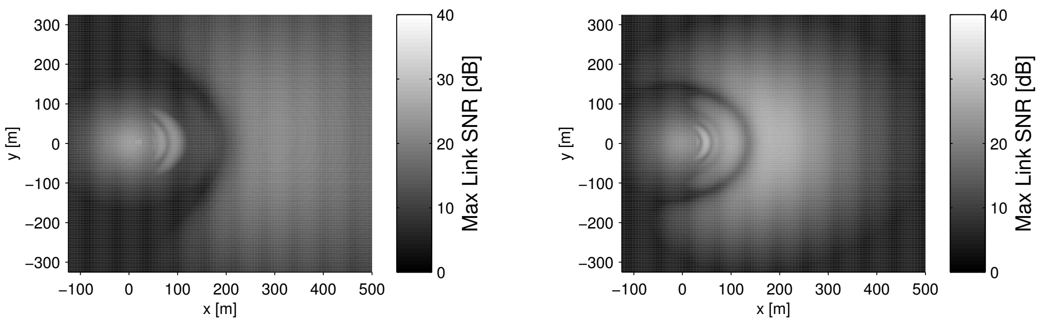

(a) $\Theta = 6°$.

(b) $\Theta = 12°$.

Figure 2.6.: Impact of downtilt at a single cell. The simulation assumes an NLOS channel. The simulation parameters are the same as SL 4 (Table A.1). However, only a single cell is evaluated.

The previous Section 2.1.2.3 discussed the importance of antenna downtilt as a lever to impact the coverage area of a BS. Figure 2.6 shows the received power at a BS depending on the UE location for $\Theta = 6°$ and $\Theta = 12°$. A lower downtilt provides better coverage, while a larger downtilt reduces the radiated field outside the cell area and is, therefore, a means to reduce inter-cell interference. The trade-off between these two goals and its impact on the performance of different detection schemes is also subject of field trials in [2].

The antenna downtilt also affects the pathloss difference of a UE to different BSs which is referred to as link separation LS. In order to investigate the impact of specific UE locations in the area of two neighboring cells and the variation in the parametrization of the pathloss model on link separation, a toy scenario of two BSs is considered, as shown in Figure 2.2b. The inter-site distance is $d_{\text{site}} = 750$ m, and UE_1 is located on the line between BS_1 and BS_2 at a distance $d_{1,1}$ to BS_1. In this case, the link separation equals the pathloss difference which, using the model in Equation (2.2), is

$$\text{LS}(d_{1,1}) = 10\eta \left(\log_{10}(\underbrace{d_{\text{site}} - d_{1,1}}_{d_{2,1}}) - \log_{10}\left(d_{1,1}\right) \right) \text{ [dB]}, \tag{2.12}$$

for isometric antennas at the UE and BSs. Figure 2.7a shows this value for different values of the pathloss exponent η. Obviously, a clear LOS link ($\eta = 2$) leads to reduced link separation, while NLOS links have a larger separation due to larger η.

Link separation for a particular antenna downtilt applied at both BSs is given by

$$\text{LS}_\Theta(d_{1,1}) = 10\eta \log_{10}\left(\frac{d_{\text{site}} - d_{1,1}}{d_{1,1}}\right) + \underbrace{A_\Theta\left(0, \theta(d_{1,1})\right)}_{A_{1,1}} - \underbrace{A_\Theta\left(0, \theta(d_{\text{site}} - d_{1,1})\right)}_{A_{2,1}} \text{ [dB]}. \tag{2.13}$$

Figure 2.7b shows the effect of the vertical antenna pattern for different values of Θ (the same downtilt is applied at both BSs). Larger downtilts result in better link separation at the cost of higher absolute pathloss (lower SNR) at the cell edge, as illustrated in Figure 2.6. Certainly, a larger downtilt can still be very effective for conventional systems, which is also shown in [GJF+08]. For CoMP systems, however, increasing the downtilt might also increase link separation in the cooperation cluster and ultimately reduces the cell area where CoMP can be applied effectively.

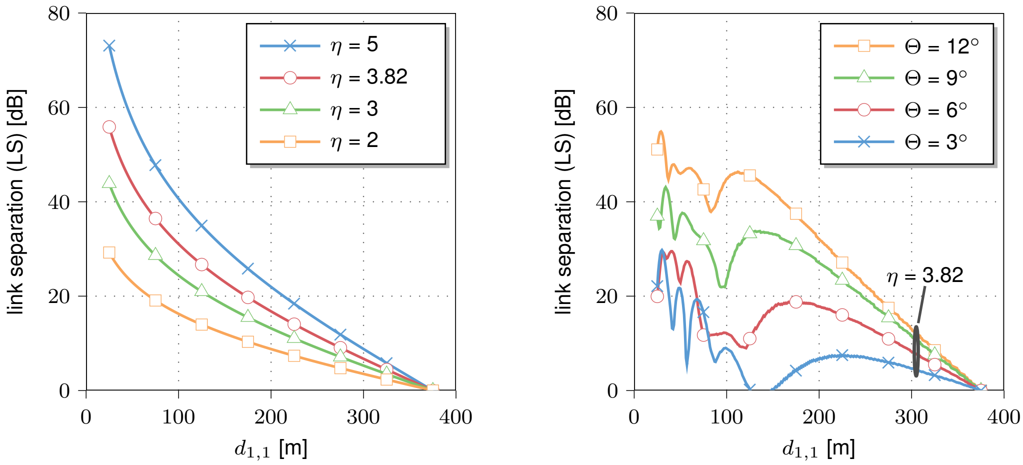

(a) Isometric antenna. **(b)** Kathrein 80010541 antenna.

Figure 2.7.: Link separation in a toy scenario of two BSs and a single UE for an isometrical and a directive [Kathrein 80010541] BS antennas with different downtilts Θ (applied at both BSs) and pathloss coefficients η. The inter-site distance is $d_{\text{site}} = 750$ m.

In conclusion, a larger downtilt is often chosen in conventional systems in order to avoid inter-cell interference. CoMP systems make use of strong links of one UE to several BSs at the additional benefit of good coverage up to the cell edge. At the same time, the downtilt settings should not reduce the performance of conventional systems too much for a fair comparison between conventional and CoMP system. For this reason, a compromise of $\Theta = 9°$ is used in most simulation models throughout this thesis.

2.1.3. Random Pathloss Due to Shadowing

As described earlier, terrestrial propagation is impacted by the particular geometries of the surrounding. The pathloss models for LOS and NLOS propagation described in Section 2.1.1.2 provide values for the average pathloss in a specific environment. The propagation in a real area is, however, not homogeneous. Instead, average pathloss is superimposed by random fluctuations due to shadowing by neighboring objects. This section describes models for these fluctuations.

2.1.3.1. Random Occurrence of LOS and NLOS and Shadowing

Section 2.1.1.2 introduced pathloss models for LOS and NLOS propagation. In a real scenario, either LOS or NLOS channels occur at different UE locations. The probability of LOS $\mathcal{P}_{\text{LOS}}$ could depend on multiple factors such as distance, BS and UE height, as well as the height of surrounding buildings. In the 3GPP urban macro model [3GP10, Table B.1.2.1-2], it is modeled by

$$\mathcal{P}_{\text{LOS}} = \min\left(18/d_{m,k}, 1)\right) \cdot \left(1 - e^{-d_{m,k}/63}\right) + e^{-d_{m,k}/63}. \tag{2.14}$$

Figure 2.8a shows a simulation result which considers the aspect of LOS probability. The pathloss at LOS locations is computed using (A.1), (A.2), and at NLOS locations using (2.5). The link towards the serving BS is LOS at about 24.6% of the locations. These LOS locations are clearly visible due to lower pathloss exponents. As a result of stochastic pathloss, a BS (which is not the closest in distance) could still serve a UE, if it happens to have an LOS channel while the closest BS is in NLOS. As a consequence, the areas served by a particular BS are no longer contiguous, which potentially causes frequent handovers. Also, the maximum coverage distance of a cell is increased for LOS which is relevant when considering time synchronization as discussed in Section 4.3.1.

Shadowing is another aspect which is related to the signal being blocked by objects in the transmission path. Based on experimental studies [IP83, OOKF68, PAN10], fading due to shadowing, also referred to as slow fading, is typically modeled by an additional log-normally distributed random loss factor

$$\text{PL}_{m,k} = \overline{\text{PL}}_{m,k}^{\text{NLOS}|\text{LOS}} + \Psi \text{ [dB]}, \tag{2.15}$$

where $\Psi \sim \mathcal{CN}\left(0, \sigma_\Psi^2\right)$. Shadow fading depends on the characteristics of the physical environment. Typical standard deviation values are $0 < \sigma_{\Psi,\text{LOS}} < 6$, and $6 < \sigma_{\Psi,\text{NLOS}} < 10$. The simulation in Figure 2.8b considers NLOS/LOS pathloss as well as shadowing. For LOS channels, the standard deviation of shadow fading is $\sigma_{\Psi,\text{LOS},1} = 4$ dB below and $\sigma_{\Psi,\text{LOS},2} = 6$ dB above the breakpoint distance, respectively. The standard deviation for NLOS channels is $\sigma_{\Psi,\text{NLOS}} = 8$ dB. Hence, the impact of shadowing is quite substantial. The pathloss in Figure 2.8b fluctuates even at very short distances because the simulation does not consider that shadowing as well as the occurrence of LOS channels are correlated over distances on the order of sizable structures such as buildings as described in the following section.

2.1.3.2. Spatial Correlation of Shadowing

The correlation properties of shadow fading have been investigated in [Gud91, Gia96, PN04]. The correlation distance can be large, especially along street tunnels, or very short in, e.g., parks where LOS is blocked by sparsely populated trees.

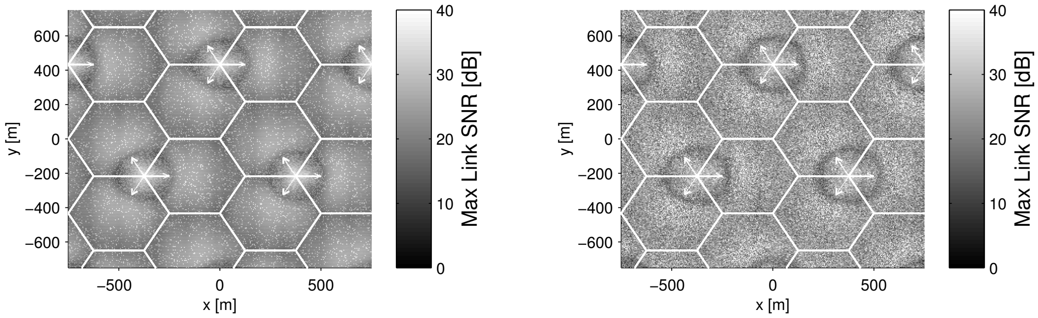

(a) Honeycomb considering LOS probability (SL 5 in Table A.1)

(b) Honeycomb considering LOS prob. and shadowing (SL 6 in Table A.1)

Figure 2.8.: Pathloss simulations that include shadowing. The simulation model of Figure 2.8b is used in the following wherever nothing else is stated explicitly.

The general effects of shadow fading correlation are now studied in a model with two BSs and a single UE as shown in Figure 2.2b. The UE in this setup is assumed to be located on a line between the BSs. The location of a UE on the line between the two BSs is described by $d_{1,1}$, the distance to BS_1. The distance to BS_2 takes the form $d_{2,1} = d_{\text{site}} - d_{1,1}$.

The simulated received power at the two BSs is shown in Figure 2.9a, assuming a shadowing correlation distance $d_{\text{shad}} = 50$ m and a shadow fading $\sigma_\Psi = 8$. Isometrical antennas are considered in order to differentiate shadowing from fading due to the antenna pattern. The correlation distance affects the handover frequency for moving UEs. Moving from BS_1 to BS_2, three handovers would occur in the example shown in Figure 2.9a. Large correlation distances reduce the handover probability as shown in [Pol97].

Shadowing of the links between one UE and multiple BSs is typically correlated as well. Figure 2.9b shows a realization of cross-correlated shadow fading with a correlation coefficient of $\rho_{\text{SF}} = 0.9$. The two shadow fading realizations are modeled using a Cholesky factorization approach [KM99]. A more complex model for the cross correlation between different channels is given in [Gra78]. Therein, the cross-correlation coefficient ρ_{SF} depends on $d_{m,k}$, d_{shad}, and the angle-of-arrive difference, ϕ_{AAD}. Intuitively, the cross-correlation coefficient is typically high when two BSs see the UE with the same azimuthal angle $\phi_{\text{AAD}} \approx 0°$, as in the case of intra-site cooperation, because the LOS will very likely be blocked by the same object. On the other hand, maximum decorrelation occurs (on average) when the UE is between the two BSs, i.e., $\phi_{\text{AAD}} \approx 180°$. Shadow fading of two UEs measured at one BS is also correlated, if they are less than d_{shad} apart. In computer simulations, this can, for example, be achieved by computing correlated shadow fading for the complete area by applying a model for 2D shadow fading [XG03] and using these realizations for a UE at a particular location. The large complexity and parameter space of shadow fading correlation make the investigation of this aspect very complex. For this thesis, it was, therefore, decided to keep the study of shadow fading correlation to a minimum and to not investigate hand-overs in CoMP systems.

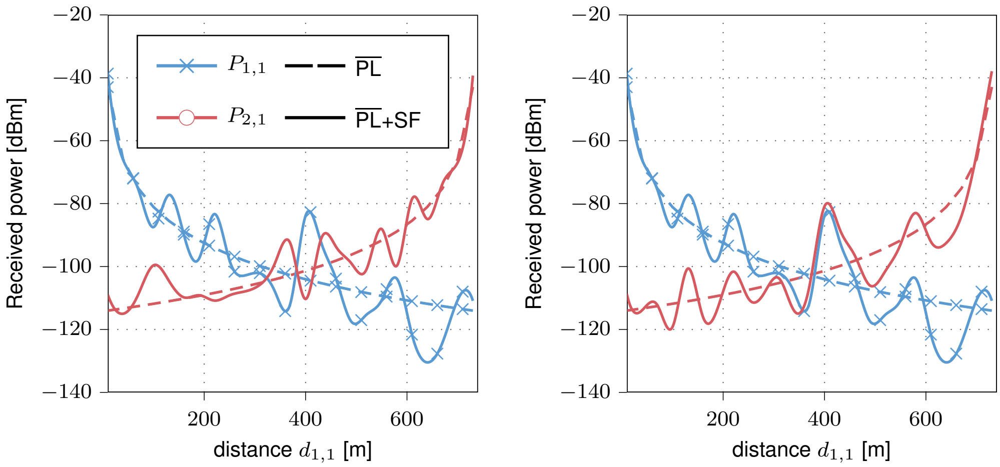

(a) No correlation of shadowing at different BSs.

(b) Correlated shadowing $\rho_{\text{SF}} = 0.9$.

Figure 2.9.: Pathloss and shadow fading realization for a toy scenario of two BSs with isometrical antennas (other parameters SL 2 Table A.1).

2.1.4. Multi-Path Propagation

Local variations (fading) of received power are caused by two effects: shadowing and multi-path propagation due to reflections from surrounding buildings or natural structures. The wireless propagation channel is a linear system which is characterized by the channel impulse response (CIR). Due to movements of the UEs, or other changes in the surroundings, cellular channels are time varying, and thereby, resulting in:

$$h(\tau, t) = \sum_i a_i(t)\delta(\tau - \tau_i(t)), \tag{2.16}$$

where a_i is the amplitude, and τ_i is the delay of the i^{th} channel path.

In a block based scheme (such as OFDM), the channel is measured for every block of duration T_{O}. The channel is typically assumed to be static during the transmission of one block. Almost all signal processing is done in the discrete baseband (see Section 2.3). Due to sampling, channel paths within one sample time $T_\mathrm{s} = \frac{1}{f_\mathrm{s}}$ cannot be resolved and are superimposed on one another, resulting in a discrete model of equally spaced channel taps

$$\underline{h}_o = \left[h_o[0], h_o[1], \ldots, h_o[\mu^{\max} - 1]\right], \tag{2.17}$$

where o is the block index, and a maximum delay $\mu^{\max} = \frac{\tau_{\max}}{T_\mathrm{s}}$ is assumed [TV05, Sec. 2.2.3]. The duration between the first and the last (non-zero) channel tab is referred to as delay spread τ^{DS}. The delay spread only differs from the maximum delay if some of the first channel tabs are zero.

The constructive or destructive superposition of many asynchronous paths in one tap might completely change the received power at distances less than a wavelength, which is an effect referred to as fast fading [Gol05, Chap. 3], [PM08, Chap. 5]. A commonly used model for fast fading was developed by Clarke [Cla68]. The model is based on the simplifying assumption of N plane waves arriving at the antenna with a uniform azimuth distribution, where their phases are arbitrary (uniformly distributed), and their amplitudes are identical. The resulting fading process has a complex circularly symmetric Gaussian distribution with a Rayleigh distributed amplitude. Channels at close proximity to one another are correlated. A movement of a UE with a speed of v causes a maximum Doppler shift of $f_\mathrm{D} = \frac{f_\mathrm{c} v}{c_{\mathrm{light}}}$. In Clarke's model, this Doppler shift results in a 50% channel coherence time of $t_{\mathrm{coh}} = \sqrt{\frac{9}{16\pi f_\mathrm{D}^2}}$ which relates to a coherence distance of $d_{\mathrm{coh}} = \sqrt{\frac{9}{16\pi}}\lambda_\mathrm{c}$.

The average sum of the power of all paths in each tap is the power delay profile (PDP):

$$\underline{\sigma}_h^2 = \left[\mathcal{E}_o[h_o[0]^2], \mathcal{E}_o[h_o[1]^2], \ldots, \mathcal{E}_o[h_o[\mu^{\max}]^2]\right]. \tag{2.18}$$

The PDP is constant over larger distances (on the order of d_{shad}). In system level simulations, the normalized PDP is typically assumed to be a constant characteristic of the complete area (see e.g. [3GP11, Table 4.1]). In order to model the PDP for a particular link, it is denormalized by scaling using the pathloss as determined in Section 2.1. Throughout all wideband channel simulations in this chapter, the typical urban (TU) PDP model, as specified in [3GP12, Table 5.2], is used. This model is characterized by 20 taps with a delay spread of $\tau^{\mathrm{DS}} = 2.14\,\mu$s. Depending on the system bandwidth (receiver resolution), multiple taps might fall into the same sample. If all channel taps lie in the same sample ($\mu^{\mathrm{DS}} = 1$), the channel is a random scalar (flat channel). The maximum bandwidth of a flat channel equals the coherence bandwidth $B_c \approx \frac{1}{\tau^{DS}} = 467$ kHz. On the other hand, a channel is frequency selective if $\mu^{DS} > 1$. The TU channel at a sampling rate of $f_s = 30.72$ MHz (20 MHz LTE channel) has $\mu^{DS} = 67$ taps.

At LOS locations (see Section 2.1.3.1), the PDP has to be adapted to account for an additional (typically strong) LOS path which reduces fading. The resulting Ricean amplitude distribution is characterized by the K-factor, which is the ratio of the non-fading LOS power and the fading NLOS power [PM08, Project 5.2]. In the 3GPP Urban Macro model (which is also used in simulations herein), the K-factor at LOS locations is log-normally distributed with a mean of 9 dB and a variance of 3.5 dB, in order to account for different degrees of LOS [3GP10, Table B.1.2.2.1-4].

2.1.5. MIMO Channels

The combination of multi-path propagation and mobility causes fading of wireless links. For MIMO systems, fading of different antennas may by uncorrelated to some extend even if antennas are close together (at distances in the order of the wavelength). This enables the spatial re-use of spectrum within one cell provided that appropriate detection algorithms for MIMO channels are used. The assumption of uncorrelated channels, which is often made in research papers, is not accurate in many cases. A more realistic simulation of MIMO channels, on the other hand, is very complex. The degree of correlation depends on the multi-path environment (angle of arrival / angle of departure) and antenna characteristics (antenna spacing, directivity). A very sophisticated model for MIMO channels, which is also used in 3GPP, is the spatial channel model [3GP11], [Kha09].

Nonetheless, uncorrelated fading of all simulated links is assumed throughout this work which is motivated as follows. The testbed used in this thesis consists of single antenna UEs, and BSs having $N_{bs} = 2$ antennas each. The two BS antennas are cross-polarized, which provide orthogonal channels in LOS scenarios, given that the antennas of two different UEs are orthogonally polarized as well [JBTJ12]. The orthogonality of different polarizations is lost in NLOS channels due to polarization dependent scattering [JTJ09, JTB+08]. In the NLOS case, however, uncorrelated channel fading was verified by Asplund et. al, [ABH+07], who measured a correlation coefficient of 0.07 for the two polarizations in a field trial. Links towards separated BS or UE antennas are assumed to be uncorrelated due to a large distance. The assumption of uncorrelated links in BSs that are collocated at the same site cannot be motivated in general. The deployment at different sites differs substantially which will be addressed in Chapter 4. For more information on this topic, the reader is referred to [PM08, Chap. 10].

2.2. Multi-Cell Signal Propagation and Joint Detection CoMP

Signal propagation across cell borders causes inter-cell interference which mutually impacts communications. This was already demonstrated in the evaluation of the toy scenario in Figure 2.7. Effective spatial signal separation is possible through partial re-use of spectral resources. In this scheme, clusters of N_{ru} neighboring cells are formed. Each of these cells uses different orthogonal transmission resources. Since this scheme allows controlling inter-cell interference to achieve a high SINR across the whole coverage area, it is beneficial in coverage limited systems with minimum signal quality requirements, such as telephony in GSM [LM01]. On the downside, partial resource re-use reduces the maximum data throughput by $\frac{1}{N_{\mathrm{ru}}}$.

With the increasing demand for mobile broadband communications, a major quality of service requirement is the satisfaction of the rapidly increasing data rate demand of new devices and services. Wherever the data rate demand exceeds its provision, a cell is capacity limited instead of coverage limited, and reusing resources in every cell promises the highest average area spectral efficiency. In a conventional system, UE signals are decoded at independent BSs. This works well as long as the UEs are located close to their serving BS as shown in Figure 2.10a. At the cell edge, however, data rates are limited by inter-cell interference which is illustrated in Figure 2.10b. A major problem of universal frequency re-use is, therefore, impaired fairness because achievable data rates depend on the UE location.

This section introduces CoMP as a potential means to combat, or even exploit, inter-cell interference. By providing sufficient backhaul capacity, received signals from multiple BSs can be exchanged to a joint decoder as depicted in Figure 2.10c. Provided that appropriate MIMO algorithms are applied, the joint decoder can potentially turn interference into useful signal energy, enabling higher average data rates and better spatial data rate distribution (fairness) in the cell area. The separation of UE signals is illustrated in Figure 2.10d. In the following, the difference between conventional detection (CD) and JD is explained in detail and both concepts are evaluated and compared in toy scenarios using information theoretic tools.

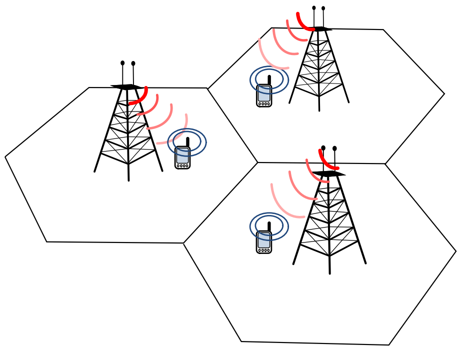

(a) No substantial interference when UEs are close to their serving BS.

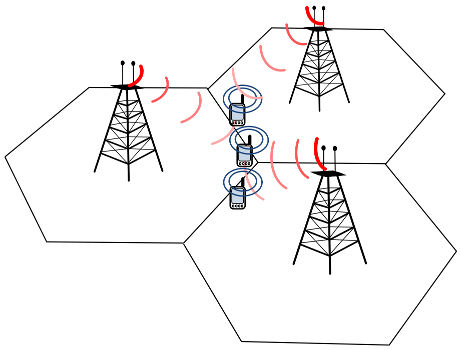

(b) Interference limites data rates of UEs at the cell edge.

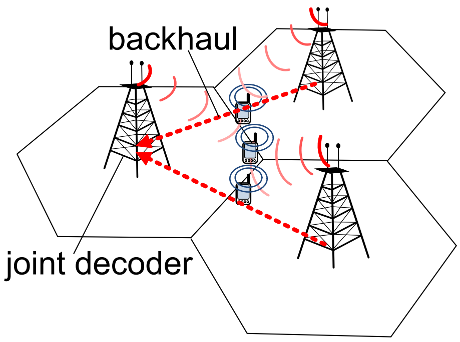

(c) BS in a CoMP system forward received signals to a joint decoder.

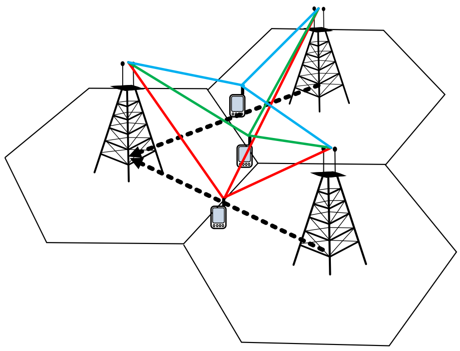

(d) The joint decoder uses MIMO detection to cancel interference.

Figure 2.10.: Introduction of JD CoMP which is used to circumvent the interference limitation of data rates in re-use one systems.

2.2.1. Information Theoretic Evaluation of Communications Performance

Information theory offers many effective tools for the evaluation of communication schemes and channels. The interest in information theoretical results increased with the dawn of modern coding techniques, which are practically feasible and operate close to the theoretic Shannon limit [Sha48]. In particular, information theoretic results for multi-user scenarios have gathered increased attention, showing that the current cellular setup with independent sources and receivers is suboptimal compared to setups that permit cooperation on the mobile and/or the base station side [KFV06, Wyn94]. Information theoretic tools are used in this section to investigate the performance of JD and CD with the goal of establishing an understanding of potential JD gains and identifying the most important channel characteristics that impact JD performance.

Table 2.1.: Simulation parameters for algorithm evaluation in different toy scenarios (TSs). Other parameters are listed in SL 4 or SL 5 in Table A.1.

	TS 1	TS 2	TS 3
type	sym	asym	sym
number of UEs	$K = 2$	$K = 2$	$K = 3$
number of BSs	$M = 2$	$M = 2$	$M = 3$
number of BS antennas	$N_{\text{bs}} = 1$	$N_{\text{bs}} = 1$	$N_{\text{bs}} = 2$
inter-site distance	$d_{\text{site}} = 750$ m		
minimum distance from serving BS	50 m		
maximum distance from serving BS	350 m		
number of UE positions	1000		
number of channel realizations per position	50		

2.2.2. System Model

A system, which consists of K single antenna UEs and M BSs with N_{bs} antennas each, is examined, as depicted in Figure 2.2a. The total number of BS antennas is denoted by $N_{\text{BS}} = M \cdot N_{\text{bs}}$. In the following, $\mathcal{K} = \{1, \ldots, K\}$ refers to the set of UEs that share the same resources. The set $\mathcal{M} = \{1, \ldots, M\}$ contains the indices of all BSs in the system. Three different scenarios are considered:

1. Symmetric scenarios where two UEs are placed in two different cells with the same distance to the cell edge;
2. Asymmetric scenario of two UEs and two BSs. UE_1 is placed in arbitrary distance to the cell edge while UE_2 is placed at the cell edge;
3. Symmetric scenario where three UEs are placed in three different cells with the same distance to the cell edge.

The simulation parameters are summarized in Table 2.1. Figure 2.11 shows the SNR at the serving BS for the $M = 2$ and $M = 3$ setups. Note that the beam peaks of the antennas in the setup of two BSs face each other (see Figure 2.11a) while they do not face each other in the setup of three BSs (Figure 2.11b).

A low mobility scenario is considered in all simulations where the channel can be assumed to be quasi-static, i.e., constant during the transmission of a codeword. The transmission from the UEs to the BSs is disturbed by additive zero-mean white Gaussian noise (AWGN) with variance σ_v^2, which is a simplified model to capture effects such as thermal noise, and RF impairments. All rate results presented in the following are derived for a normalized bandwidth and power and are, therefore, measured in bits per channel use (bpcu) or transmitted symbol, which is equivalent to bits/s/Hz (when, overhead for reference and control signals is not considered). Since the probability of the occurrence of a data rate in bps across the entire bandwidth is equally likely and sampling at the Nyquist frequency is assumed, the rate results are de-normalized by multiplication with the signal bandwidth B.

Each UE sends one independent Gaussian codeword at fixed power p. While the transmission of single Gaussian codewords is not necessarily capacity achieving for the interference channel [Kob81, MK09], it is at least as good as any modulation and coding scheme (MCS) currently used in LTE [MNK+07]. Conventional LTE uplink power control adjusts the received power at the serving BS. This approach is less effective in CoMP systems since a UE is served by multiple cells with different pathloss [NKHS09]. More sophisticated power control schemes which are optimized for JD exist [YCHT10]. Fixed transmit power is applied in this work in order to simplify the field trial system. However, this choice is also a good compromise between LTE power control which favors CD and CoMP power control which favors JD.

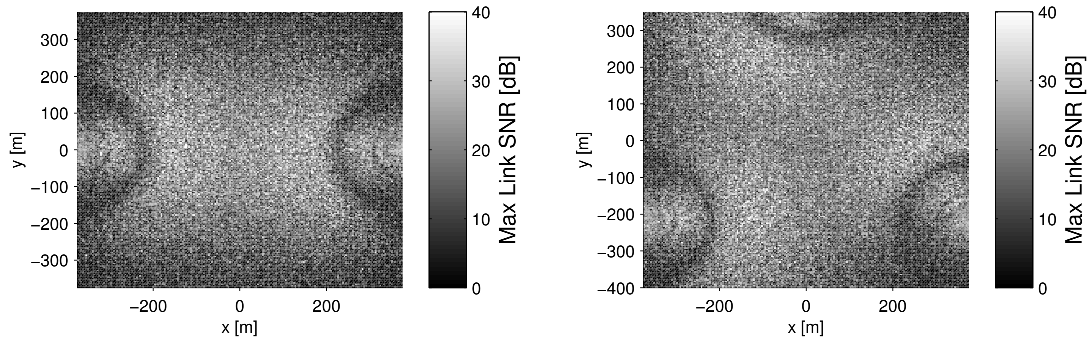

(a) Setup of 2 BSs. **(b)** Setup of 3 BSs.

Figure 2.11.: SNR in the coverage area of the toy scenario models considered in the information theoretic evaluation of this section. The pathloss models is parameterized as listed in SL 7 (Table A.1)

2.2.3. Conventional Detection (CD)

The UEs share the same resources. Therefore, BSs receive a linear superposition of all UE signals. Assuming a flat channel (for what will later be introduced as a subcarrier), the transmission model for symbols received at BS$_m$ can be represented by

$$\underline{Y}_m = \sum_{k\in\mathcal{K}} \underline{H}_{m,k} X_k + \underline{V}_m, \tag{2.19}$$

where $\underline{Y}_m \in \mathbb{C}^{[N_{\text{bs}} \times 1]}$ is a received symbol vector, the noise vector $\underline{V}_m \in \mathbb{C}^{[N_{\text{bs}}]}$ is a realization of a zero-mean circularly symmetric complex Gaussian (ZMCSCG) random process $\mathcal{CN}\left(\underline{0}_{N_{\text{bs}}}, \mathbf{\Phi}_v\right) = \mathcal{CN}\left(\underline{0}_{N_{\text{bs}}}, \sigma_v^2 \mathbf{I}_{N_{\text{bs}}}\right)$, and $X_k \sim \mathcal{CN}(0, p) \in \mathbb{C}$ is a Gaussian transmit symbol. The random channel realization $\underline{H}_{m,k} \in \mathbb{C}^{[N_{\text{bs}} \times 1]}$ includes slow fading (pathloss) and fast fading. A Rayleigh channel is assumed, and the elements in $\underline{H}_{m,k} \sim \mathcal{CN}\left(\underline{0}_{N_{\text{bs}}}, \overline{\text{pl}}_{m,k} \cdot \mathbf{I}_{N_{\text{bs}}}\right)$ are assumed to be uncorrelated, as motivated in Section 2.1.5.

For conventional detection (CD), UEs are (potentially) decoded at different serving BSs. Their signals at all other BSs cause interference. Due to Gaussian codebooks, this interference can be modeled as additional (colored) Gaussian noise with covariance $\underline{H}_{m,k}\, p\, (\underline{H}_{m,k})^H$. Assuming a model (as shown in Figure 2.2b) where $K = M$ UEs are located in different cells and decoded at their particular serving BS ($k = m$, i.e., UE_1 is decoded at BS_1), the largest reliable transmission rate of UE_k is the mutual information between the input sequence and the channel output sequence which, in [CT06, Chap. 15], is shown to be

$$r_k^{\text{CD, MMSE}} = I\left(\underline{Y}_{m=k}; X_k\right) = \log_2\left(1 + p\underline{H}_{m,k}^H \left(\sum_{k'=\mathcal{K}\backslash k} \underline{H}_{m,k'} p \underline{H}_{m,k'}^H + \mathbf{\Phi}_v\right)^{-1} \underline{H}_{m,k}\right), \; k \in \mathcal{K}. \tag{2.20}$$

The largest reliable sum rate is given by

$$r_{\text{s}}^{\text{CD, MMSE}} = \sum_{k \in \mathcal{K}} r_k^{\text{CD, MMSE}}. \tag{2.21}$$

Note that, the expression in Equation (2.20) assumes the decoding BS to have channel knowledge of all UEs and to take the interference of other UEs into account in the linear minimum mean square error (MMSE) detection filter. This scheme is referred to as interference rejection combining (IRC) in 3GPP. This benchmark is chosen for comparing JD to the best possible decoding at a BS that operates independently. More details on MIMO detection are given in Section 3.3.3.

The rates at particular UE locations depend on the random Rayleigh fading channel realizations. The average performance of different communication schemes is, therefore, compared on the basis of the ergodic rate $\bar{r}$, which is determined by averaging over many channel realizations at the same location. The location dependent ergodic UE rates and the sum rate are depicted in Figure 2.12 for the $K, M = 2$ Setup shown in Figure 2.11a. The average SNR at the cell edge is about

15 dB. The BSs are equipped with $N_{\text{bs}} = 1$ antenna each. Figure 2.12a shows the results of the symmetric scenario (TS 1 in Table 2.1 where the UEs are located in their serving cell and have the same distance to the cell edge, which is located at distance $d_{\text{CE}} = \frac{d_{\text{site}}}{2}$ between the BSs. Due to the symmetric setting, ergodic rates of both UEs are the same. The fluctuations of rates that occurs when both UEs are between 50-150 m away from their serving BS are caused by the antenna pattern and can also be seen in Figure 2.7b. In most of the cell area, the rates are less than 5 bpcu. The rate at the cell edge would be about 1 bpcu if the interference was as strong as the signal energy. Due to fading, however, the rates can be larger which results in a larger average of about 1.2 bpcu. Interestingly, the rates within the cell can be very similar to the ones at the cell edge due to the impact of the antenna pattern.

The UE rates in an asymmetric scenario are shown in Figure 2.12b. In this scenario, the location of UE_1 is varied between its serving BS and the cell edge while the location of UE_2 is fixed at the cell edge ($d_{2,2} = d_{\text{CE}}$). Despite its fixed location, the rate of UE_2 decreases with $d_{1,1}$ because UE_1 moving towards BS_2 causes more interference. The general behavior of $\bar{r}_1^{\text{CD, MMSE}}$ is the same as in Figure 2.12a, but the rates are smaller because of the strong interference from UE_2 at the cell edge.

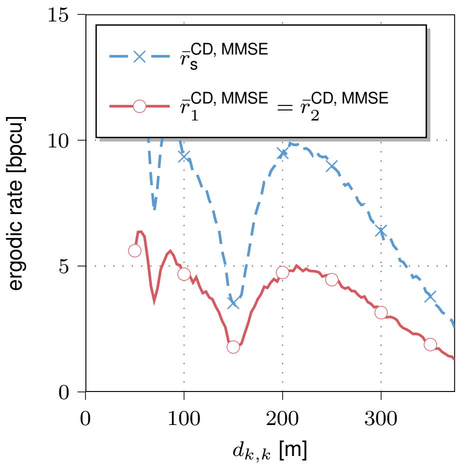

(a) Rates for a symmetric scenario (TS 1).

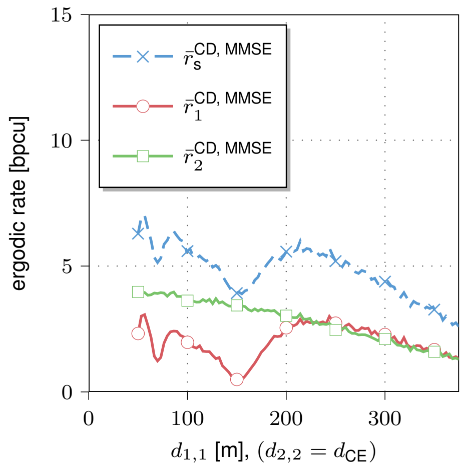

(b) Rates for a asymmetric scenario (TS 2)

Figure 2.12.: Ergodic UE rates as well as sum rates for CD at different UE locations ($M = K = 2,\ N_{\text{bs}} = 1$). Shadowing is not considered in these simulations (parameters as in SL 4 in Table A.1). The same simulation results that include a different realization of shadow fading at each locations are shown Figure A.1.

2.2.4. Joint Detection

The term uplink joint detection (JD) refers to receiver algorithms where received signals of multiple BSs are evaluated jointly for enhanced detection performance through interference control. JD requires the exchange of received signals to a central processing unit. In this section, a decoding cluster is formed from all BSs $C = M$ in the system, which are assumed to be connected through an error-free and unconstrained backhaul [MF11d]. The channel from the kth UE to all BS antennas is denoted by $\underline{H}_k = \left[\underline{H}_{1,k}^T, \ldots, \underline{H}_{M,k}^T\right]^T$, which allows the transmission to be modeled as

$$\underline{Y} = \underbrace{\left[\underline{H}_0 \quad \cdots \quad \underline{H}_K\right]}_{\boldsymbol{H}} \underline{X} + \underline{V}, \tag{2.22}$$

where $\underline{Y} \in \mathbb{C}^{[N_{\text{BS}}]}$, $\underline{V} \in \mathbb{C}^{[N_{\text{BS}}]} \sim \mathcal{CN}\left(\underline{0}_{N_{\text{BS}}}, \boldsymbol{\Phi}_v = \sigma_v^2 \mathbf{I}_{N_{\text{BS}}}\right)$, and $\boldsymbol{H} \in \mathbb{C}^{[N_{\text{BS}} \times K]}$.

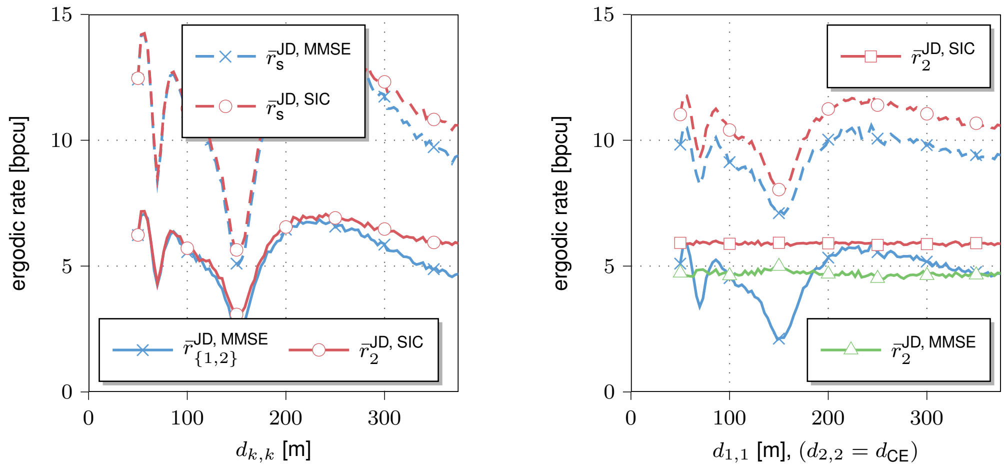

(a) JD rates for a symmetric scenario (TS 1).

(b) JD rates for an asymmetric scenario (TS 2)

Figure 2.13.: Rate of the two individual UEs as well as the sum rate for linear MMSE and SIC detection. For SIC, UE_1 is decoded first and UE_2 second. Shadowing is not considered in these simulations (parameters as in SL 4 in Table A.1).

The maximum sum capacity of all UEs is that of a multiple access channel which, in [CT06], is shown to be

$$r_{\text{s}}^{\text{JD}} = I(\underline{Y}; X_0, \ldots, X_K) = \log_2 \left| 1 + \sum_{k=1}^{K} \underline{H}_k^H \boldsymbol{\Phi}_v^{-1} \underline{H}_k \right| . \tag{2.23}$$

The capacity of this channel ($\mathcal{R}_{\text{JD}}$) is not a single number but a region of data rates that are jointly achievable [CT06, Chap. 10]. It is defined by a set of inequalities that are satisfied by each point in the region:

$$\mathcal{R}_{\text{JD}} = \left\{ (r_1, \ldots, r_K) : \sum_{k \in \mathcal{K}'} r_k^{\text{JD, ML}} \leq \log_2 \left(1 + \sum_{k \in \mathcal{K}'} p \underline{H}_k^H \mathbf{\Phi}_v^{-1} \underline{H}_k \right), \forall \mathcal{K}' \right\}, \tag{2.24}$$

where $\mathcal{K}'$ is any tuple of UE indices. The rates in this region can be achieved through maximum likelihood (ML) decoding. An alternate approach to achieve the sum capacity of the multiple access channel is successive interference cancellation (SIC) in combination with MMSE MIMO detection. The messages are decoded in one of $K!$ orderings $\underline{\pi}$, whose each element is a permutation of the set $\{1, \ldots, K\}$. Assuming the ordering $\underline{\pi}^{[1]}$ (with elements $\pi_1^{[1]} = 1$, $\pi_2^{[1]} = 2, \ldots$), the rate of the first decoded message satisfies

$$r_1^{\text{JD, SIC}} = I\left(\underline{Y}; X_1\right) = \log_2 \left(1 + p \underline{H}_1^H \left(\sum_{k'=2}^{K} \underline{H}_{k'} p \underline{H}_{k'}^H + \mathbf{\Phi}_v \right)^{-1} \underline{H}_1 \right). \tag{2.25}$$

This rate is achieved using a linear MMSE equalization filter which will be described in Section 3.3.3. After successful decoding, the interference from this message is canceled to get the symbols $\underline{Y}' = \underline{Y} - \underline{H}_1 X_1$. The maximum rate of the second data stream is given by

$$r_2^{\text{JD, SIC}} = I\left(\underline{Y}'; X_2\right) = I\left(\underline{Y}; X_2 | X_1\right) = \log_2 \left(1 + p \underline{H}_2^H \left(\sum_{k'=3}^{K} \underline{H}_{k'} p \underline{H}_{k'}^H + \mathbf{\Phi}_v \right)^{-1} \underline{H}_2 \right). \tag{2.26}$$

The messages of all other UEs are decoded, in the same way, after canceling the interference of all previously decoded messages. For any ordering $\underline{\pi}$, the rate of the k^{th} decoded message is given by

$$\begin{aligned} r_{\pi_k}^{\text{JD, SIC}} &= I\left(\underline{Y}; X_{\pi_k} | X_{\pi_{k-1}}, \ldots, X_{\pi_1}\right) = \\ &\log_2 \left(1 + p \underline{H}_{\pi_k}^H \left(\sum_{k'=k+1}^{K} \underline{H}_{\pi_{k'}} p \underline{H}_{\pi_{k'}}^H + \mathbf{\Phi}_v \right)^{-1} \underline{H}_{\pi_k} \right). \end{aligned} \tag{2.27}$$

The maximum sum rate $r_{\text{s}}^{\text{JD, SIC}} = \sum_k r_k^{\text{JD, SIC}}$ is independent of the decoding order. For a proof of this result, the reader is referred to [CT06, Theorem 2.2.1]. Interference cancellation is a complex algorithm which, if required, can be omitted for linear MMSE detection of each UE's signal, which results in achievable rates given by

$$r_k^{\text{JD, MMSE}} = I\left(\underline{Y}; X_k\right) = \log_2\left(1 + p\underline{H}_k^H \left(\sum_{k'=\mathcal{K}\setminus k}^{K} \underline{H}_{k'} p \underline{H}_{k'}^H + \mathbf{\Phi}_v\right)^{-1} \underline{H}_k\right). \quad (2.28)$$

The UE rates and sum rates for both linear as well as SIC detection are shown in Figure 2.13. The same symmetric and asymmetric scenarios as in the case of CD are considered. The message of UE$_1$ is always decoded first. Thus, the linear rates of UE$_1$ are the same as the SIC rates. The benefit of SIC is well illustrated in the symmetric scenario. While UE$_2$ and UE$_1$ achieve the same rate for linear detection, comparing $r_2^{\text{JD, MMSE}}$ and $r_2^{\text{JD, SIC}}$, demonstrates the gain of SIC. The benefit of SIC is largest when both UEs are located at the cell edge where interference is the major rate limiting factor.

2.2.5. Comparison of Conventional and Joint Detection

The benefit of JD compared to CD is clearly visible when comparing the results shown in Figure 2.12a and Figure 2.13a. At the cell edge, where interference poses as the major rate limiting factor, JD achieves a 4-fold increase in the sum rate. The gain is smaller when UEs are located closer to their serving BS. The performance of JD and CD is compared further in Figure 2.14, which shows the rate CDF results for two different symmetric setups: the one in Figure 2.14a and Figure 2.14b consists of $M = K = 2$; the other in Figure 2.14c and Figure 2.14d of $M = K = 3$ BSs and UEs. In contrast to Figure 2.12a and Figure 2.13a, the simulation model also considers shadowing. For each scenario, two different results are displayed. The curves in the sub-figures to the left depict the CDFs of (instantaneous) rates for a single channel realization, which assumes coding over a static and flat channel. The curves in the sub-figures to the right show the CDFs of average (ergodic) rates that are achieved at individual UE position. Thus, this case assumes coding over many fading realizations (at a constant pathloss and shadowing). The different shape shows the impact of small scale fading on achievable rates.

Comparing the two scenarios considered in Figure 2.14, the relative gains of JD are comparable, but they are slightly higher for the three cell scenario due to the higher total interference. On average, instantaneous and ergodic rate are the same. The average rate for JD MMSE in Figure 2.14a is 5.93 bpcu compared to 3.99 bpcu for CD MMSE. Due to the averaging involved, ergodic rates are less likely to be very low, but also less likely to be very high. In both cases, the relative gains of using

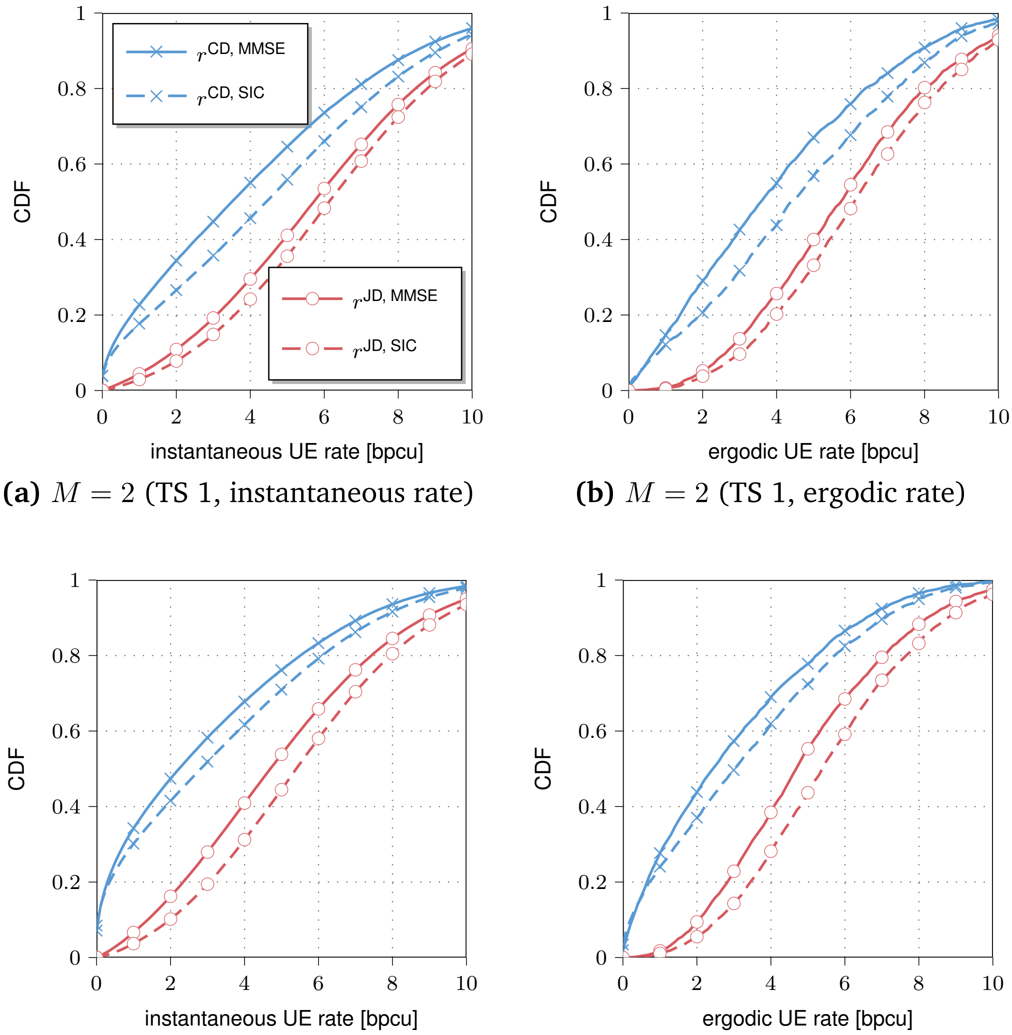

(a) $M = 2$ (TS 1, instantaneous rate)

(b) $M = 2$ (TS 1, ergodic rate)

(c) $M = 3$ (TS 3, instantaneous rate)

(d) $M = 3$ (TS 3, ergodic rate)

Figure 2.14.: Rate CDFs for CD and JD in two different scenarios based (parameters of the channel model are listed in SL 5 in Table A.1).

JD are larger at the cell edge (low rates), where JD achieves about three times the rate of CD. In order to achieve a fair comparison of SIC rates, this technique is also considered for CD. The application of SIC for CD, however, requires that UEs are decoded at the same BS. Except when the UEs are located in the same cell, this would typically not be the BS with the lowest pathloss for all UEs. SIC for CD is, therefore, beneficial only as long as the benefit from canceling interference is larger than the rate loss due to a lower link SNR, which is the case when both UEs are located close to the cell edge. If they are located near their serving BS, linear detection at separate BSs achieves better performance. This will be considered again in Section 3.3.3. The scheme for $r^{\text{CD, SIC}}$ is optimal in the choice of where the

UEs are decoded. When the UEs are decoded at the same BS, SIC is applied, and when they are decoded at different BSs linear MMSE detection is applied. For SIC, the detecting BS is always the one which receives the UE signals at the higher sum SNR. This aspect will be considered again in Section 3.3.3. The average rate of CD SIC is 4.62 bpcu and JD SIC achieves an average rate 6.31 bpcu. Consequently, the JD gain is about 37%. The same results for the asymmetric scenario are shown in Figure A.2 in Appendix A.3.

The average rate of CD SIC in TS 3 (Figure 2.14c and Figure 2.14d) is 3.42 bpcu while JD SIC achieves 5.62 bpcu which is a gain of about 67%. The lower absolute rates in the $M = K = 3$ scenario are a consequence of the lower cell edge SNR, which is only 10 dB (see Figure 2.11b). The higher JD CoMP gains compared to the one observed for $M = K = 2$ result from the stronger interference in a scenario with three UEs.

2.3. Broadband Communications and Hardware

The previous sections discussed the characteristics of channels in cellular systems as well as information theoretic results for CD and JD. The results shown are based on idealistic assumptions especially regarding coding/decoding complexity, fading channels, and channel estimation and, therefore, serve only as performance upper bounds. However, significant progress in digital communications was made in recent decades, which allows approaching theoretical bounds. A major breakthrough was the discovery of low complexity coding/decoding schemes that almost achieve the Shannon bound for the additive white Gaussian noise (AWGN) channel, in particular Turbo [BGT93] and LDPC [Gal62] codes. While such codes are also successfully applied to broadband multi-user cellular systems, these system pose many additional challenges, namely:

- fading and cross-coupling of transmit symbols in time, frequency, and space which requires sophisticated methods for symbol detection.
- interference between signals of different users.
- the requirement that the current channel state has to be estimated.
- dealing with potential transmission (decoding) errors due to channel state information (CSI) impairments, or limited codeword length.

As a consequence, today's systems use the available spectrum well below the maximum efficiency. The authors of [MCR11] showed that 3G (HSDPA) systems utilize only about 40% of the available channel capacity. Major loss factors are pilots, guard carriers, coding, equalization, and channel estimation.

Multiple modulation schemes for digital wireless broadband communication were developed, each a different compromise regarding complexity, spectral efficiency, latency, max. velocity, and coverage. One such scheme, which is widely used in many modern communications systems, is OFDM. This section addresses the application of OFDM to cellular systems and highlights the subtleties of the application of OFDM to CoMP systems and major impairments that might limit performance. The reader is referred to e.g. [Gol05],[TV05] for a basic mathematical description of OFDM. Detailed explanations of the specific OFDM signal processing chain used in the field trial setup are given in Chapter 3.

2.3.1. OFDM Basics

The main notion of OFDM is the conversion of a high rate (bandwidth) single carrier system into multiple orthogonal low rate (bandwidth) subcarrier signals. For multipath channels, the orthogonality of subcarriers is preserved by inserting a cyclic prefix. Consequently, the convolution by the multi-path channel is converted into a multiplication with the channel transfer function (CTF), i.e., parallel transmissions on orthogonal subcarriers in the frequency domain.

Due to the orthogonality of subcarriers, they can be modulated and demodulated independently and in parallel. These properties significantly reduce the complexity of channel estimation and equalization (symbol detection) for (MIMO) broadband systems and facilitate efficient hardware implementation. The channel on a subcarrier and OFDM symbol for a system of K transmit and N_{BS} receive antennas is fully described by a coupling matrix $\boldsymbol{H} \in \mathbb{C}^{[N_{\mathrm{BS}} \times K]}$ as used in Section 2.2.1. The OFDM approach is also very favorable for multi-user communications because individual UEs can transmit on neighboring subcarriers without mutual interference as long as frequency and time synchronization is achieved. The scheduler can assign frequency resources dynamically for UEs to transmit on subcarriers which are in a good fading state for achieving multi-user diversity gains [DCF12].

2.3.2. OFDM Hardware Implementation and Application to Cellular Systems

A block diagram of the basic OFDM signal processing architecture is depicted in Figure 2.15. Such wireless transceivers for data communication are implemented partly in a digital baseband signal processor and partly in an analog front-end. Most of the processing, including coding/decoding, modulation/demodulation, channel estimation, and synchronization is done in the digital baseband. The functions in the analog front-end include digital to analog converter (DAC)/analog to digital converter (ADC), and filtering in order to reduce out of band radiation, up/down conversion, and power amplification.

2.3.2.1. Non-Ideal Analog Front-Ends

Assuming ideal analog components, the functions at the transmitter and receiver are complementary. In real front-ends, however, impairments which affect the analog transmission chain are

- thermal noise and interference.
- carrier frequency offset (CFO), sampling clock offset, phase noise of the phase locked loop (PLL) [Pet05].
- quantization noise and clipping in the DAC/ADC [HB08, Sec. 4.5].
- phase and amplitude imbalances in the complex (IQ) signal streams [Win07].

These impairments can be evaluated and (partially) compensated for in the digital baseband [FLP+05]. Not all impairments are significant in a particular system. Depending upon the radio frequency (RF), baseband, and channel characteristics; it is, therefore, important to identify and evaluate those impairments that critically limit performance.

2.3.2.2. Asynchronous Reception in Time

Signals propagate at the speed of light c_{light}. Assuming LOS, they are, therefore, received after some propagation delay $\tau_{m,k} = \frac{d_{m,k}}{c_{\text{light}}}$. In the uplink, UEs align their timing at the serving BS through a timing advance mechanism for transmission of UEs located at greater distance to their serving BS. The BSs in an CoMP cluster are potentially not collocated. Therefore, a UE cannot align signal reception at each of them. Since the serving BS is typically the one in shortest distance, the signal received at all other BSs is delayed. The time delay of arrival (TDOA) of UE$_k$ in a cluster of several BSs $\mathcal{C}$ is

$$\Delta\tau_k = \frac{\max_{m\in\mathcal{C}} d_{m,k} - \min_{m\in\mathcal{C}} d_{m,k}}{c_{\text{light}}}. \tag{2.29}$$

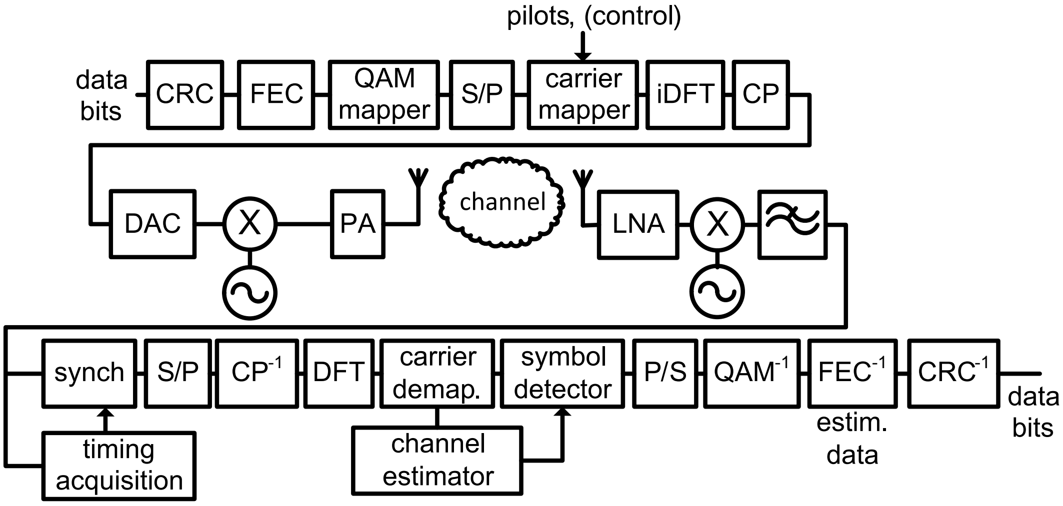

Figure 2.15.: OFDM system block diagram. Abbreviations used in this figure are: forward error correction (FEC), cyclic prefix (CP), power amplification (PA), low noise amplifier (LNA), serial-to-parallel conversion (S/P).

The largest TDOAs that occur depend not only on the inter-site distance and the cluster size, but also on shadowing because a UE might connect to a BS further away if this BS happens to be in LOS as was discussed in Section 2.1.3. From the BS's perspective, the timing of received signals is measured relative to a reference time. When UEs are received with an symbol timing offset due to TDOAs in a CoMP setup which potentially impairs the signal quality. Using OFDM, however, a certain timing misalignment may be tolerated. To illustrate this, the OFDM (symbol) timing (discrete Fourier transform (DFT) window timing) of all BSs is assumed to be aligned, and all UEs synchronize their OFDM timing with their serving BS. Figure 2.16 illustrates the timing of two UE signals received at BS_1. In the example, BS_1 is the serving BS of UE_1. A synchronization tolerance of τ_{est} should guarantee that inaccurate synchronization (estimation errors of the optimal timing point) causes OFDM symbols to be received prior to the receiver OFDM timing ($\tau < 0$), which would result in inter-symbol interference (ISI). Thus, UE_1 is received with a delay $\tau = \tau_{\text{est}}$. UE_2, on the other hand, aligns its timing towards another serving BS, which is not collocated at the same site of BS_1. Due to the TDOA, the symbol received at BS_1 is delayed by some symbol timing offset $\tau_{1,2}$. The symbols of both UEs should be processed in the same receive block (DFT window) in order to avoid ISI. At the same time, the cyclic prefix also needs to cover the channel decay between two successive OFDM symbols, which is marked by A in Figure 2.16. Assuming a maximum delay spread of $\tau^{\text{DS}} = 1.42\ \mu$s which is later to be found out a the typical value in an urban environment and provisioning a synchronization tolerance of $\tau_{\text{est}} = T_{\text{CP}}/8 = 0.58\ \mu$s, the maximum inter-site distance is

$$d_{\text{site}}^{\max} = c_{\text{light}} \left(T_{\text{CP}} - \left(\underbrace{\tau^{\text{DS}} + \tau_{\text{est}}}_{2\ \mu s} \right) \right) \approx 810\ \text{m}, \tag{2.30}$$

for a cyclic prefix length of $T_{\text{CP}} = 4.7\ \mu$s.

CoMP for larger inter-site distances is investigated in [Kot12] which shows that timing misalignment causes impairments. These impairments can be eliminated using highly complex algorithms, and significant mitigation is possible using appropriate less complex signal processing algorithms that are feasible using today's technology. Since symbol timing offsets at the BSs are also caused by misalignment of UEs and BSs, as well as multi-path propagation effects (delay spread), measurements will show if such signal processing techniques ought to be considered in real urban multi-cell scenarios, which are the subject of this work.

2.3.2.3. Channel Estimation

The mobile channel is subject to fading as described in Section 2.1.4. The rate at which uncorrelated channel states occur is the correlation time. In order to estimate the current channel state, pilot symbols are inserted into the transmitted signal at defined positions in the time frequency grid. Noise and other impairments of non-ideal front-ends affect the data as well as the reference symbols which are required for channel estimation. Accurate channel knowledge, however, is vital for the correct estimation of data symbols. In a multi-user MIMO system (such as uplink JD), the channel of multiple UEs needs to be estimated using orthogonal reference symbols to gain accurate knowledge of the full channel matrix $\boldsymbol{H}$. Thus, the signaling overhead increases with the cluster size.

2.4. Summary and Conclusions

- Cellular systems are very complex due to the wide range of applications, devices, use cases (vehicular, indoor, etc.), and the complexity of the mobile wireless channel in general.

- System design, development, and standardization relies on extensive simulation studies in modeled environments. Simulation models need to capture the effects of pathloss, the impact of antennas, shadowing, propagation, multi-antenna propagation incl. antenna correlation and polarization.

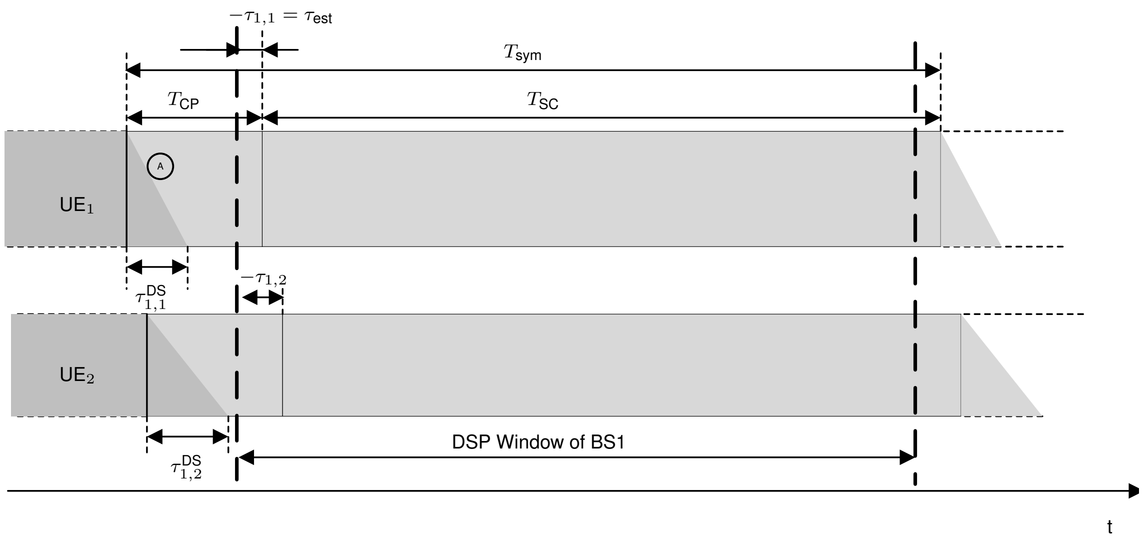

Figure 2.16.: OFDM symbol timing

- Simulation results are very accurate and reliable when network functions are progressed in successive incremental steps. In this case, models and their parameterization can be developed and validated in existing system implementations. The experience accumulated is a source of confidence for innovations. The approach, however, is very problematic when significant aspects of the cellular system structure are envisioned to be radically re-engineered.

- CoMP as a groundbreaking approach to significantly increase spectral efficiency. CoMP techniques completely change the fundamental notion that each UE communicates with just one particular serving BS. Instead, multiple clustered BSs cooperate for JD of multiple UEs that would otherwise, in a conventional system, cause substantial mutual interference.

- Information theoretic analysis and simulation show average gains to be in the order of 35 – 70%, and much larger at the cell edge which increases fairness. CoMP is, therefore, suggested as a means towards ubiquitous access and homogeneous system performance which is the ultimate goal of mobile operators.

- However, current simulation models need to be verified in field trials in order to verify that simulation models capture all important aspects for the reliable evaluation of CoMP, multi-cell propagation in particular. In addition, the application of certain algorithms are based on critical assumptions.

For example, the orthogonality of subcarriers in OFDM relies on perfect synchronization in time and frequency as well as on ideal (linear) hardware components such as amplifiers, mixers, and ADCs.

- It was shown that the assumption of synchronization might either not hold for cooperative BSs (time synchronization) or requires additional efforts (frequency and time synchronization). The identification of the most relevant effects and their compensation at the receiver is addressed in the following chapters.